A&A 409, 715–735 (2003)
DOI: 10.1051/0004-6361:20031110

Astronomy & Astrophysics

Mass-loss from dusty, low outflow-velocity AGB stars⋆

I. Wind structure and mass-loss rates

J. M. Winters[1,2], T. Le Bertre[2], K. S. Jeong[2], L.-Å. Nyman[3,4], and N. Epchtein[5]

[1] IRAM, 300 rue de la Piscine, 38406 St. Martin d'Hères, France
[2] LERMA, UMR 8112, Observatoire de Paris, 61 Av. de l'Observatoire, 75014 Paris, France
[3] Swedish-ESO Submillimetre Telescope, European Southern Observatory, Casilla 19001, Santiago 19, Chile
[4] Onsala Space Observatory, 439 92 Onsala, Sweden
[5] Observatoire de la Côte d'Azur, BP 4229, 06304, Nice Cedex 4, France

Received 26 March 2003 / Accepted 14 July 2003

Abstract. We present the first results of a CO(2–1), (1–0), and 86 GHz SiO maser survey of AGB stars, selected by their weak near-infrared excess. Among the 65 sources of the present sample we find 10 objects with low CO outflow velocities, $v_{\rm exp} \lesssim 5\,{\rm km\,s^{-1}}$. Typically, these sources show (much) wider SiO maser features. Additionally, we get 5 sources with composite CO line profiles, i.e. a narrow feature is superimposed on a broader one, where both components are centered at the same stellar velocity. The gas mass-loss rates, outflow velocities and velocity structures suggested by these line profiles are compared with the results of hydrodynamical model calculations for dust forming molecular winds of pulsating AGB stars. The observations presented here give support to our recent low outflow-velocity models, in which only small amounts of dust are formed. Therefore, the wind generation in these models is dominated by stellar pulsation. We interpret the composite line profiles in terms of successive winds with different characteristics. Our hydrodynamical models, which show that the wind properties may be extremely sensitive to the stellar parameters, support such a scenario.

Key words. hydrodynamics – stars: mass-loss – stars: AGB and post-AGB – stars: winds, outflows – radio lines: stars

1. Introduction

It is well established, that stars of low and intermediate initial mass ($0.8\,M_\odot \lesssim M_{\rm i} \lesssim 6$–$8\,M_\odot$, Blöcker 1999), after central hydrogen and helium exhaustion, finally evolve through the Asymptotic Giant Branch (AGB) phase in the Hertzsprung-Russell diagram. During that phase, the stars become unstable against large amplitude pulsations (e.g., Ledoux & Walraven 1958; Ledoux 1958; Ostlie & Cox 1986). Thereby, shock waves are injected into the stellar atmosphere which by dissipation of their momentum and energy lead to a substantial density enhancement of the atmospheric gas compared to a hydrostatic stratification (e.g., Wood 1979; Bowen 1988). The resulting increased density in regions of comparably low temperatures provides favorable conditions for the formation of complex molecules and possibly even for the formation of small solid particles (dust grains), which, by their strong coupling to the stellar radiation field are able to drive a massive wind (e.g., Fleischer et al. 1992). Therefore, pulsating AGB stars are often surrounded by dense circumstellar shells. The material in these shells, mainly molecular gas, is flowing outward with typical velocities in the range 10–30 km s^{-1} (e.g., Nyman et al. 1992), causing the star to loose mass at typical rates in the range $\sim 10^{-7}$–$\sim 10^{-4}\,M_\odot\,{\rm yr}^{-1}$ (e.g., Loup et al. 1993).

Both, from theoretical considerations (e.g., Gail & Sedlmayr 1987; Dominik et al. 1990) and from observations (e.g., Epchtein et al. 1987; van der Veen & Habing 1988) it has been argued, that this mass-loss phenomenon could only exist above some minimum mass-loss rate of the order of $10^{-7}\,M_\odot\,{\rm yr}^{-1}$ and for luminosities exceeding a minimum value of the order of $10^4\,L_\odot$. However recently in the ISOGAL survey, Omont et al. (1999) have discovered a new population of AGB sources in the Bulge of our Galaxy with low mass-loss rates ($\sim 10^{-8}\,M_\odot\,{\rm yr}^{-1}$) and low luminosities ($\sim 3 \times 10^3\,L_\odot$).

During the last decade, a consistent theoretical description has been developed to model spherical, dust forming outflows from a molecular atmosphere excited by periodic pulsations (Fleischer et al. 1992, 1995). This model accounts well for the observed properties of outflows from luminous red giants (e.g., Winters et al. 1994, 1997, 2000a). On its basis, we have explored systematically the dependence of the outflow characteristics on the stellar parameters (Winters et al. 2000b). We find two dynamically different regimes for the spherical

Send offprint requests to: J. M. Winters,
e-mail: winters@iram.fr

⋆ Based on observations obtained at the European Southern Observatory, La Silla, Chile and at the IRAM, Pico Veleta, Spain.

outflows: Models in the first regime, A, are characterized by outflow velocities in excess of $5\,\mathrm{km\,s^{-1}}$, and mass-loss rates larger than $3 \times 10^{-7} M_{\odot}\,\mathrm{yr^{-1}}$. These winds are driven by radiation pressure on dust. Due to the strong, non-linear coupling of the dust component to the thermo- and hydrodynamical structure these models develop an instability which leads to an eigen-timescale of the shell resulting in an onion-like layered structure of the circumstellar shell (Fleischer et al. 1995; Höfner et al. 1995). The models in the second regime, B, produce low mass-loss rates, $\dot{M} \lesssim 3{\times}10^{-7}\,M_{\odot}\,\mathrm{yr^{-1}}$, at low outflow velocities, $v_{\rm exp} \lesssim 5\,\mathrm{km\,s^{-1}}$. These winds are produced, e.g., by low stellar luminosities. In these models due to the lower gas densities, only a small amount of dust forms, which translates to a lower dust-to-gas ratio. Therefore, pulsation becomes important in these models as a direct driving mechanism for the mass-loss which, together with radiation pressure on dust, generates a tenuous wind.

The separation of the winds into these two regimes is controlled by the value of the radiative acceleration in the sonic region of the wind. To establish a radiation driven wind, the ratio, α, between outward directed radiative force and inward directed gravitational force has to exceed unity. For a dust driven wind, this is the case in the dust formation zone, located at about 3 stellar radii in a region of comparably high densities, thus producing high mass-loss rates (models of type A). The models of type B stay below the critical value of $\alpha = 1$ and, therefore, do not produce dust driven winds but require the additional momentum input provided by shock wave dissipation to produce a tenuous outflow. Since the value of α is determined by the stellar parameters, a star evolving along the AGB could change between both states, e.g., by increasing its luminosity or by decreasing its temperature it could move from region B to A, i.e. change from a low mass-loss rate state to a high mass-loss rate state, or vice versa.

From the observational side there are indications that some long-period variables may have indeed a low expansion velocity. Knapp et al. (1998) acquired CO rotational line spectra with a very good signal-to-noise ratio and found evidence for composite profiles with a narrow peak superimposed on a broader one. They interpret these profiles as resulting from 2 successive winds with different expansion velocities and different ages. The slow wind typically has a $v_{\rm exp} \leq 5\,\mathrm{km\,s^{-1}}$ and a mass-loss rate $\dot{M} \leq 5 \times 10^{-7}\,M_{\odot}\,\mathrm{yr^{-1}}$. Young (1995) carried out a volume limited ($d \leq 500\,\mathrm{pc}$) survey of Miras and found several sources with an expansion velocity $\leq$5 $\mathrm{km\,s^{-1}}$. Finally, Kerschbaum et al. (1996) measured $v_{\rm exp} = 1.9\,\mathrm{km\,s^{-1}}$ for the Semi-Regular (SR) variable $\mathrm{L^2}$ Pup and found several other SRs with expansion velocities in the range 6 to 8 $\mathrm{km\,s^{-1}}$. SiO 86 GHz maser observations of $\mathrm{L^2}$ Pup show, that the photospheric material in this source is moving at a velocity of about $10\,\mathrm{km\,s^{-1}}$ (Haikala 1990; Haikala et al. 1994; Winters et al. 2002), much higher than the terminal wind outflow velocity. The high photospheric velocities and simultaneously slow envelope expansion of $\mathrm{L^2}$ Pup can be well explained by our low mass-loss rate models (Winters et al. 2002). This conclusion is supported by independent evidence based on 11.7 and 17.9 μm images of the $\mathrm{L^2}$ Pup circumstellar shell obtained with the Keck I telescope by Jura et al. (2002), who also suggest that $\mathrm{L^2}$ Pup could be taken as a prototype of red giants undergoing low mass-loss rates with low expansion velocities.

Such low mass-loss rate AGB stars may have important implications for evaluating the mass injection rate into the Interstellar Medium (ISM), since current estimates of the mass-loss rate, e.g. for the ISOGAL sources, are based on infrared color indices, assuming a "standard" outflow velocity of $15\,\mathrm{km\,s^{-1}}$. By such an approach, the derived mass-loss rate scales linearly with the (assumed) outflow velocity of the wind and inversely with the dust-to-gas mass ratio (e.g. Groenewegen 1997; Le Bertre 1997). The mass-loss rate of objects like $\mathrm{L^2}$ Pup therefore would be overestimated by at least a factor 5.

Our initial objective was to check whether there exist in nature objects with properties corresponding to those found for our B-type models, i.e. low outflow velocity in the wind, low mass-loss rate, and comparably high, time variable photospheric velocities. The dynamical structure which can be inferred for the $\mathrm{L^2}$ Pup outflow already gave a positive hint. Our main goals are now to describe the characteristics of these low velocity, low mass-loss rate winds and to study the properties of the stars, in order to understand the mass-loss processes acting in these sources, and finally to evaluate the contribution of such objects to the replenishment of the ISM.

In order to achieve this task, we undertook a survey in the CO($J = 2{-}1$) and ($J = 1{-}0$) rotational lines of nearby sources which show only a weak near-infrared excess. For part of the sample we also obtained 86 GHz SiO ($v = 1$, $J = 2{-}1$) maser observations. The selection of our sample is described in Sect. 2 and the observations are described in Sect. 3. We present our results in Sect. 4 and discuss their relation to the hydrodynamical models in Sect. 5. In Sect. 6 we present our conclusions.

2. Selection of the sample

We aimed to obtain CO rotational line spectra of dusty, low luminosity AGB stars to estimate their mass-loss rates and wind velocities and to compare them with the predictions of our hydro-models.

From the CO(1–0) survey of Nyman et al. (1992, their Fig. 3), there is an indication that sources with low expansion velocities are found preferentially in the region II of the IRAS [12−25, 25−60] color diagram (van der Veen & Habing 1988). This indicates that they correspond to circumstellar shells with small optical depth, a fact which agrees with our theoretical models. However the IRAS criterion is not selective enough because sources with low outflow velocity are still a minority in region II (see Fig. 3 in Nyman et al. 1992).

Earlier we had performed a survey of bright sources at 2 μm in the southern galactic plane ("Valinhos survey") and obtained for ∼630 objects *JHKLM* photometry with the ESO 1-m telescope (Epchtein et al. 1987). Most of these sources were also detected by IRAS. The combination of all these data allows a classification (a, b, c, etc.) of ∼560 bright 2 μm stellar sources. The class "b" contains ∼230 sources with a weak near-infrared excess as compared with the IRAS fluxes ($K{-}L' \sim 0.5$, $L'{-}[12] \sim 1.3$). The properties of the "b" sources which have been optically

identified (~40) fit well those of long-period variables with low expansion velocities (see Young 1995; Kerschbaum et al. 1996; Knapp et al. 1998) and those expected from our theoretical models.

In the present project, we reassess the sources belonging to the Nyman et al. sample and for which we have obtained *JHKLM* photometry (Fouqué et al. 1992) which allows to classify them in the "b" type. This selection gives 165 sources of which only 17 had been detected in CO(1–0) by Nyman et al. (1992) at the SEST. These detections were used to validate our approach. Still, we kept these 17 sources in our sample in order to obtain CO(1–0) spectra with higher signal to noise ratio using the new SEST receivers, and also to obtain CO(2–1) data. Additionally, we obtained data for 40 sources with the IRAM 30 m telescope. Therefore, we expect a much higher detection rate than in the former observations by Nyman et al. (1992). In fact, of the 23 sources detected with the SEST in the current survey, 20 objects were detected also in the (1–0) line, but for some of them the (1–0) detection could only be ascertained by the (2–1) spectrum evaluation. All sources are at $\delta < +20^\circ$, $|b^{\rm II}| \geq 5^\circ$ and have a $F_{25\,\mu{\rm m}} > 20$ Jy. The first limit comes from the Fouqué et al. sample, which has been observed from La Silla. The second limit ensures a limited contamination by interstellar emission lines and the third one favors nearby and/or bright sources which should be more easily detected.

At the present stage of our program, 65 sources, out of 165, have been observed (Sect. 3, Table 1), of which 59 have been detected in CO(2–1) (Table 2).

3. Observations

We observed 25 sources (19 M-stars, 2 C-stars, 2 S-stars, and 2 of unknown chemical type) with the SEST in CO(2–1) and CO(1–0), of which 23 were detected in CO(2–1) and 20 in CO(1–0). The Mira KK Car was not detected and the (2–1) spectrum of CC Ind showed two possible lines at $v_{\rm lsr} = -20.5\,{\rm km\,s^{-1}}$ and $64\,{\rm km\,s^{-1}}$ but with a low signal-to-noise ratio (see Fig. 24). The results on L^2 Pup have already been reported in Winters et al. (2002). The data were obtained in two runs, on September 28/29, 2001 and on May 15/17, 2002. We used SIS receivers at 230 GHz and 115 GHz and typical system temperatures above the atmosphere were 300 and 500 K, respectively. The beam width of the telescope is 50″ at 3 mm and 23″ at 1.3 mm. The observations were done in a dual beam switch mode with a beam throw of 11.5′. The intensities reported here are given in main beam brightness temperature, $T_{\rm mb}$, which is the chopper wheel corrected antenna temperature, T_A^*, divided by the main beam efficiency, $\eta_{\rm mb}$. The main beam efficiency is 0.7 and 0.5 at 3 mm and 1.3 mm, respectively. Three acousto optical spectrometers were used simultaneously, one high resolution (HRS) with a bandwidth of 86 MHz, a channel separation of 43 kHz, and a resolution of 80 kHz, the other two are low resolution spectrometers (LRS) with bandwidths of about 1 GHz, channel separations of 0.7 MHz, and resolutions of 1.4 MHz. As compared to Nyman et al. (1992), our detection rate is higher because the system has been improved and because the sources are brighter in CO(2–1) than in CO(1–0); 12 sources which then were not detected have now clearly been detected with the SEST. In most cases, we have observed the sources in our SEST sample only in CO(2–1) and (1–0); the two exceptions are L^2 Pup and *o* Ceti which have been observed also in SiO at 86 GHz ($v = 1$, $J = 2-1$) with the HRS mode.

With the IRAM 30 m telescope, simultaneous observations of CO(2–1) and (1–0) emission and SiO maser emission at 86 GHz were performed in the flexible observing mode by various observers for 40 sources (39 O-rich, 1 unknown) in December 2001 and in March, October, and December 2002. 36 of these sources were detected in the CO(2–1) line and 25 in the SiO maser line. The CO non-detections are SU Eri, S Crt, V1293 Aql, and (possibly due to instrument problems) V533 Oph. At IRAM, SIS receivers have been used with a low-resolution filter bank (resolution 1 MHz, bandwidth 0.5 GHz) and a high-resolution filter bank (resolution 100 kHz, bandwidth 25.3 MHz) for the CO(2–1) line, and an autocorrelator for the CO(1–0) and the SiO 86 GHz line (used at a resolution of 80 kHz with a bandwidth of 140 MHz). Typical system temperatures (on the main-beam brightness scale) were 130 K at 86 GHz, 450 K at 115 GHz, and 600 K at 230 GHz and the beam-widths (*FWHM*) are 28″ at 86 GHz, 21″ at 115 GHz, and 11″ at 230 GHz, respectively. For the observations performed in October and December 2002, the VESPA autocorrelator has been used to obtain CO(2–1) high resolution spectra (resolution 40 kHz, bandwidth 140 MHz) and for the CO(1–0) and SiO lines (resolution 40 kHz, bandwidth 70 MHz).

The observations at the IRAM 30 m telescope were done in wobbler switching mode with a beam throw of 60″. The main-beam brightness temperatures reported here were calculated by multiplying the observed antenna temperature by the ratio of the forward to main beam efficiency, which is 1.26 at 86 GHz, 1.67 at 115 GHz, and 2.05 at 230 GHz. The SiO maser intensities are converted to fluxes by multiplying the antenna temperature by a factor $5.9\,{\rm Jy\,K^{-1}}$.

All observed sources of our sample (65) are listed in Table 1. All those (62), which have been optically identified are long-period variables of late spectral type (M, S, C). Two of the unidentified sources (IRAS 20359−3806 and IRAS 21368−3812) are likely to be oxygen-rich (their IRAS LRS class is 21). The observational results are given in Table 2, which also contains in the fifth column the detection limit for each spectrum.

4. Results

For all objects in our sample which were detected in CO, we obtained at least (2–1) spectra since the (2–1) line, due to beam filling and optical depth effects, is brighter than the (1–0) line, usually by more than a factor 2 (see Fig. 3; the exception is RZ Sgr with an intensity ratio of only 1.48). There are 7 sources (ZZ Ari, V352 Ori, GL Mon, Z Cnc, RT Hya, RT Cnc, V Aqr) which have been observed at IRAM and which have not been detected in the (1–0) line, in our SEST sample we have 3 such sources (X Hor, TV Sco, and CC Ind). Because of the higher line intensity, the S/N ratio of the (2–1) spectra is usually higher than for the (1–0) observations. Also, for most of our objects we obtained high resolution spectra in (2–1). Therefore, we

Table 1. List of the 65 observed sources. *C*: chemical type (M: O-rich, S: S-type, C: C-rich).

IRAS name	Name	Var.	*C*	*P* [d]	*d* [pc]	$L\star$ [$L_\odot$]	Tel.	*K* [mag]	L' [mag]
00245−0652	UY Cet	SRb	M	440	407[2]	9104	IRAM	0.20	–0.20
01438+1850	SV Psc	SRb	M	102	405[3]	6000	IRAM	0.64	0.30
01527+1656	ZZ Ari	SR	M	–	691[3]	6000	IRAM	1.80	1.52
02000+0726	RAFGL 292	–	M	–	319[3]	6000	IRAM	0.12	–0.23
02168−0312	o Cet	M	M	332	128[1]	9943	SEST	–2.41	–3.22
02234−0024	R Cet	M	M	166	570[2]	2826	IRAM	2.20	1.58
02455+1718	T Ari	SRa	M	323	322[1]	6589	IRAM	0.04	–0.38
02464−5915	X Hor	SRa	M	280	411[3]	6000	SEST	0.67	0.26
03082+1436	U Ari	M	M	371	496[2]	7419	IRAM	0.85	0.28
03489−0131*	SU Eri	SRb	M	112	398[3]	6000	IRAM	0.60	0.27
05220−0611	EX Ori	–	M	–	510[3]	6000	IRAM	1.14	0.73
05265−0443	S Ori	M	M	419	309[2]	8585	IRAM	–0.34	–0.90
05592−0221	V352 Ori	Lb	M	115	273[3]	6000	IRAM	–0.22	–0.51
06140−2729	IRC -30055	–	M	–	411[3]	6000	SEST	0.67	0.38
06333−0520	GL Mon	SRb	M	104	312[3]	6000	IRAM	0.07	–0.29
07034−3551	RAFGL 1064	–	M	–	232[3]	6000	SEST	–0.57	–0.90
07120−4433	L^2 Pup	SRb	M	141	61[1]	2431	SEST	–2.49	–3.06
07299+0825	S CMi	M	M	332	365[2]	6493	IRAM	0.33	–0.27
08189+0507	FZ Hya	Lb	M	134	354[3]	6000	IRAM	0.35	0.02
08196+1509	Z Cnc	SRb	M	104	389[1]	3273	IRAM	1.21	0.92
08236−0444		–	–	–	440[3]	6000	IRAM	0.82	0.42
08272−0609	RT Hya	SRb	M	253	272[1]	4701	IRAM	0.04	–0.39
08349−5945*	KK Car	M	M	–	342[3]	6000	SEST	0.27	–0.33
08372−0924	RV Hya	SRc	M	116	318[1]	4246	IRAM	0.49	0.16
08555+1102	RT Cnc	SRb	M	90	340[1]	6517	IRAM	0.17	–0.12
11252+1525	AF Leo	SRb	M	119	567[3]	6000	IRAM	1.37	1.02
11466−4128	X Cen	M	M	315	458[2]	6096	SEST	0.89	0.27
11501−0719*	S Crt	SRb	M	155	490[1]	7438	IRAM	0.82	0.41
12046−0629	RW Vir	Lb	M	116	422[1]	9676	IRAM	0.21	–0.11
12277+0441	BK Vir	SRb	M	150	176[1]	4593	IRAM	–0.88	–1.28
13114−0232	SW Vir	SRb	M	150	143[1]	7547	IRAM	–1.87	–2.28
13269−2301	R Hya	M	M	388	125[2]	7828	SEST	–2.20	–2.88
13492−0325	AY Vir	SRb	M	193	340[2]	3386	IRAM	0.88	0.49
14280−2952	Y Cen	SRb	M	180	320[1]	11000	SEST	–0.53	–0.90
15094−6953	X TrA	Lb	C	–	460[1]	24244	SEST	–0.60	–1.23
15223−0203	OV Ser	–	M	–	329[3]	6000	IRAM	0.19	–0.15
15410−0133	BG Ser	M	M	143	334[3]	6000	IRAM	0.22	–0.33
17102−1031	NSV 8322	–	M	–	337[3]	6000	SEST	0.24	–0.16
17265−0725	BD-07 4447	–	M	–	342[3]	6000	IRAM	0.27	–0.23
17398−4344	TV Sco	SRb	M	200	393[2]	3534	SEST	1.15	0.74
17504−0234*	V533 Oph	SR	M	32	344[1]	5704	IRAM	0.34	0.05
17539+1037	DO 4490	–	M	–	519[3]	6000	IRAM	1.18	0.78
18243+0352	V988 Oph	SRb	M	129	428[3]	6000	IRAM	0.76	0.46
18359+0847	X Oph	M	M	334	186[2]	6540	IRAM	–1.14	–1.58
19143−5032	V Tel	SRb	M	125	309[3]	6000	SEST	0.05	–0.36
19247−1722	IRC -20563	–	M	–	434[3]	6000	SEST	0.79	0.36
19267+0345	V858 Aql	Lb	M	–	697[3]	6000	IRAM	1.82	1.47
19306+0455*	V1293 Aql	–	M	–	621[1]	11838	IRAM	0.83	0.57
19510−5919	S Pav	SRa	M	386	345[1]	27972	SEST	–1.38	–1.86
20120−4433	RZ Sgr	SRb	S	223	388[2]	4028	SEST	0.98	0.62
20359−3806	SON 5115	V*	–	–	401[3]	6000	SEST	0.62	0.20
20443+0215	V Aqr	SRb	M	244	341[2]	4487	IRAM	0.58	0.18
20479+0554	NX Del	SR	M	–	616[3]	6000	IRAM	1.55	1.18
20526−5431	S Ind	M	M	400	764[2]	8120	SEST	1.69	1.01
21044−1637	RS Cap	SRb	M	340	277[2]	6681	SEST	–0.30	–0.66
21197−6956	Y Pav	SRb	C	233	360[1]	6077	SEST	0.37	–0.03

Table 1. continued.

IRAS name	Name	Var.	C	P [d]	d [pc]	$L\star$ [$L_\odot$]	Tel.	K [mag]	L' [mag]
21368−3812	RAFGL 5595	–	–	–	483[3]	6000	SEST	1.02	0.66
21377−0200	HT Aqr	SR	M	–	426[3]	6000	IRAM	0.75	0.39
21439−0226	EP Aqr	SRb	M	55	135[1]	4828	IRAM	–1.51	–1.87
22142−8454	BW Oct	V*	M	–	233[1]	4675	SEST	–0.29	–0.64
22190−0751	DZ Aqr	SR	M	–	285[1]	3774	IRAM	0.38	0.07
22196−4612	π^1 Gru	Lb	S	–	153[1]	11388	SEST	–2.17	–2.61
22540−5740	DM Tuc	V*	M	–	219[1]	3342	SEST	–0.06	–0.36
23041+1016	R Peg	M	M	378	350[1]	7929	IRAM	0.02	–0.61
23134−7031*	CC Ind	–	M	–	394[1]	11017	SEST	–0.08	–0.47

Remarks: IRAS name*: not (uniquely) detected in CO; distance[1]: Hipparcos parallax; distance[2]: P-L relation (Feast 1996; Groenewegen & Whitelock 1996); distance[3]: $L_\star$ assumed to be 6000 $L_\odot$.

determine the mass-loss rates and outflow velocities from the (2–1) observations for all our sources.

Some of the sources have been observed at different epochs. In these cases, we usually find strong temporal variations in the SiO maser profile if it has been detected for the respective source (see Table 2 and, e.g., Fig. 18). On the other hand, we don't see indications for temporal variations in the CO profiles. It should be noted however, that observations were repeated only, if the initial CO data were of insufficient quality for our purposes.

4.1. Distances and luminosities

For determining mass-loss rates by standard methods using CO rotational lines we need to know the distance to the object. For 24 sources of our sample there exist reasonably well determined Hipparcos parallaxes. For these objects, we give an estimate of the stellar luminosity in Table 1, which is derived from the objects' K magnitude (taken from Fouqué et al. 1992) and the bolometric correction in the K-band, BC_K, given in Le Bertre et al. (2001). For two sources (X TrA and S Pav) the luminosity (~25 000 $L_\odot$) derived by this method seems to be largely overestimated (see Fig. 1). Variability types and periods reported in Table 1 are generally taken from the SIMBAD database (source: Kholopov et al. 1985 (GCVS)). However, we adopt the values given by Lebzelter & Hinkle (2002) for AY Vir, AF Leo, V988 Oph, V352 Ori, RW Vir, FZ Hya, BK Vir, and EP Aqr.

Nine of our sources without a parallax are classified as Miras with known periods, of which 8 have a period longer than 150 d, and 6 of the SRb variables without a parallax have a period longer than 150 d. In these cases we have used the period-luminosity relations by Feast (1996) for M-Miras and S-stars and the P-L relation given by Groenewegen & Whitelock (1996) for C-stars to derive the luminosity. The distance is then determined from the bolometric correction in the K-band given in Le Bertre et al. (2001).

The application of a period-luminosity relation to SRs is a matter of debate. We apply here to SRbs the period-luminosity relation proposed by Feast (1996) for O-rich Miras and by Groenewegen & Whitelock (1996) for C-rich Miras, respectively. Combining DENIS and EROS data Cioni et al. (2003) find a relation for SRbs in the LMC which runs parallel to the Feast relation (their Figs. 5 and 6). Knapp et al. (2003) use Hipparcos parallaxes to investigate long-period variables in the nearby regions of the Galaxy. They find relations for both Miras and SRbs. Their Mira relation agrees with that of Feast (1996) but the SRb relation is much shallower and, moreover, has only a small correlation coefficient.

The Mira R Hya has a very uncertain Hipparcos parallax which nevertheless gives a lower limit for the distance ($d > 250$ pc). The distance ($d = 125$ pc) derived here from the P-L relation is lower than that, a discrepancy that was already noted by Knapp et al. (1998).

The average luminosity of the objects in our sample which have a relatively well determined Hipparcos parallax (excluding X TrA and S Pav) is 6700 ± 2900 $L_\odot$ while the average luminosity derived from the P-L relation is 6100 ± 2100 $L_\odot$ (see Fig. 1). Both mean values are in reasonable agreement. Although the luminosities of individual objects are obviously uncertain, we believe that the range 4000−8000 $L_\odot$ should be correct for most sources in our sample. Therefore, we adopt for the other sources of our sample (26) a luminosity of 6000 $L_\odot$ and again derive their distances from the K magnitude and the bolometric correction BC_K based on the $K - L'$ index as given in Le Bertre et al. (2001).

4.2. Velocities

To obtain the required values (expansion velocity $v_{\exp}$ and peak main-beam brightness temperature T_{mb}), we fitted a parabola to the line profiles (after a linear baseline was subtracted)

$$T(v) = T_{\mathrm{mb}} \left[1 - \left(\frac{v - v_\star}{v_{\exp}} \right)^2 \right] \quad (1)$$

where $v_\star$ (= v_{lsr}) is the stellar velocity.

We have in our sample 5 sources (SV Psc, RAFGL 292, o Cet, R Hya, EP Aqr) out of 59 detected in CO(2–1), which clearly show composite CO profiles (see Sect. 4.5.1, e.g., Fig. 11). In those cases, we determined the mass-loss rates and the outflow velocities by independent fits to each line component.

Table 2. Observational results. In general, there are two entries per source, referring to the CO(2–1) and (1–0) line, respectively. If the source shows a composite CO profile, two entries are listed for each line (i.e. one entry for each component). For CO(2–1), the values refer to the high-resolution spectrum when it has been obtained. The column "SiO" gives a label about the detection (Y) / non-detection (N) in this work of the 86 GHz maser line, "-" means, that we did not observe the line. In the comments column, "D" means "double wind", "P": parabolic profile, "R": rectangular profile, "A": asymmetric profile, "2p": double-peaked profile.

IRAS name	$v_{\rm exp}$ [km s^{-1}]	$v_{\rm lsr}$ [km s^{-1}]	$T_{\rm mb}$ [K]	rms [K]	$\int T_{\rm mb}\,{\rm d}v$ [K km s^{-1}]	$\dot{M}$ [$M_\odot$ yr^{-1}]	$R_{\rm CO}$ [10^{16} cm]	line CO	SiO	comments
00245−0652	7.50	5.00	0.400	0.104	5.00	1.06e–06	6.00	(1–0)	Y	R
–	8.00	4.50	1.700	0.128	17.59	1.20e–06	6.26	(2–1)		P
01438+1850	2.50	7.00	0.240	0.050	0.63	1.80e–07	3.32	(1–0)	Y	D, see text and Fig. 6
–	12.00	7.00	0.130	0.050	2.22	1.12e–06	5.13	(1–0)		
–	1.50	6.50	1.570	0.131	2.35	1.15e–07	3.15	(2–1)		
–	11.00	6.50	0.600	0.131	7.89	1.07e–06	5.18	(2–1)		
01527+1656	11.50	3.50	0.120	0.017	2.27	8.61e–07	4.48	(2–1)	N	LRS
02000+0726	2.00	23.25	0.140	0.047	0.40	7.83e–08	2.24	(1–0)	Y	D, see text and
–	9.50	23.25	0.380	0.047	4.78	1.11e–06	5.60	(1–0)		Figs. 7 and 8
–	2.50	23.25	0.500	0.064	1.40	1.00e–07	2.37	(2–1)		
–	9.50	23.25	0.900	0.064	11.54	8.46e–07	4.78	(2–1)		
02168−0312	3.00	46.00	1.500	0.020	4.52	3.71e–07	4.70	(1–0)	Y	
–	1.50	46.75	4.000	0.048	8.12	1.17e–07	3.17	(2–1)		D, see text and Fig. 9
–	7.00	46.75	3.000	0.048	24.60	8.27e–07	5.33	(2–1)		
02234−0024	7.50	31.50	0.150	0.042	1.94	9.05e–07	5.47	(1–0)	Y	R SiO maser
–	7.50	31.50	0.500	0.190	5.16	8.23e–07	5.17	(2–1)		P strongly variable
02455+1718	3.00	–1.00	0.200	0.071	0.79	1.66e–07	2.95	(1–0)	Y	R, see text and Fig. 12
–	3.50	–1.25	1.170	0.063	5.53	2.49e–07	3.51	(2–1)		R
02464−5915	4.50	68.50	0.078	0.014	0.39	2.28e–07	3.02	(2–1)	–	LRS
03082+1436	6.00	–54.50	0.150	0.044	1.29	5.77e–07	4.60	(1–0)	Y	SiO strongly variable
–	5.50	–54.50	0.850	0.075	6.00	6.14e–07	4.94	(2–1)		
05220−0611	5.00	–30.00	0.080	0.035	0.51	3.34e–07	3.61	(1–0)	Y	A, SiO overshoot
–	5.50	–31.00	0.550	0.089	3.84	5.04e–07	4.41	(2–1)		A
05265−0443	7.00	14.00	0.220	0.065	1.87	5.32e–07	4.13	(1–0)	Y	SiO strong
–	6.50	14.00	1.100	0.210	10.15	5.40e–07	4.29	(2–1)		
05592−0221	6.50	22.50	0.060	0.020	0.57	1.05e–07	1.66	(2–1)	N	LRS, noisy
06140−2729	9.00	–8.00	0.030	0.014	0.32	7.37e–07	4.51	(1–0)	–	bad quality
–	9.00	–4.00	0.070	0.034	0.73	5.57e–07	3.84	(2–1)		bad quality
06333−0520	4.50	–13.75	0.910	0.074	5.08	2.99e–07	3.53	(2–1)	N	see text and Fig. 13
07034−3551	10.00	–23.00	0.045	0.014	0.68	5.81e–07	3.77	(1–0)	–	R
–	11.00	–22.50	0.260	0.032	3.65	8.01e–07	4.37	(2–1)		R
07120−4433	3.50	32.00	0.074	0.017	0.32	4.47e–08	1.29	(1–0)	Y	see text and
–	3.00	33.00	0.720	0.054	3.21	5.73e–08	1.59	(2–1)		Winters et al. (2002)
07299+0825	2.50	52.00	0.300	0.113	1.09	1.81e–07	3.34	(1–0)	Y	see text and Fig. 14
–	3.80	51.00	1.100	0.125	4.21	3.08e–07	3.84	(2–1)		
08189+0507	9.00	–14.00	0.150	0.066	2.10	7.09e–07	4.41	(1–0)	N	R
–	9.50	–13.00	0.780	0.100	10.13	8.75e–07	4.88	(2–1)		R
08196+1509	8.00	–12.00	0.130	0.013	1.05	3.01e–07	2.81	(2–1)	N	LRS, barely detected
08236−0444	6.00	44.00	0.450	0.118	3.10	9.01e–07	5.96	(1–0)	N	noisy
–	5.00	44.75	1.600	0.107	10.85	6.61e–07	5.36	(2–1)		see text and Fig. 15
08272−0609	3.50	25.50	0.300	0.083	1.64	1.03e–07	2.11	(2–1)	Y	R, see text and Fig. 16
08372−0924	5.00	–43.25	0.200	0.065	0.57	3.29e–07	3.58	(1–0)	N	
–	5.00	–43.25	0.900	0.096	6.26	3.50e–07	3.70	(2–1)		see text and Fig. 17
08555+1102	12.00	29.00	0.120	0.024	1.85	4.37e–07	2.97	(2–1)	N	LRS
11252+1525	6.00	7.00	0.170	0.037	1.33	7.08e–07	5.18	(1–0)	Y	
–	6.00	7.00	0.570	0.066	4.41	6.46e–07	4.91	(2–1)		P
11466−4128	6.50	24.50	0.025	0.007	0.15	4.81e–07	4.01	(1–0)	–	very noisy
–	8.00	24.00	0.060	0.020	0.68	4.90e–07	3.73	(2–1)		LRS, very noisy
11501−0719	–	38.00	–	0.133		–	–	(2–1)	Y	SiO strong
12046−0629	8.00	22.50	0.300	0.015	2.52	1.04e–06	5.76	(1–0)	N	
–	9.00	21.00	1.200	0.060	14.19	1.22e–06	6.04	(2–1)		LRS
12277+0441	7.50	16.50	0.600	0.119	5.49	5.49e–07	4.09	(1–0)	Y	strong maser
–	6.00	16.75	3.300	0.223	26.36	4.77e–07	4.12	(2–1)		P

Table 2. continued.

IRAS name	v_{exp} [km s^{-1}]	v_{lsr} [km s^{-1}]	T_{mb} [K]	rms [K]	$\int T_{mb}\,dv$ [K km s^{-1}]	$\dot{M}$ [$M_\odot$ yr^{-1}]	R_{CO} [10^{16} cm]	line CO	SiO	comments
13114−0232	8.50	–11.50	2.000	0.158	25.61	9.81e–07	5.45	(1–0)	Y	2p, see text and Fig. 21
–	8.50	–11.50	8.000	0.283	102.82	9.81e–07	5.45	(2–1)		2p
13269−2301	9.00	–11.00	0.060	0.011	0.72	3.07e–07	2.72	(1–0)	–	
–	4.50	–10.50	0.300	0.060	1.73	1.34e–07	2.21	(2–1)		D, see text and Fig. 10
–	10.00	–10.50	0.500	0.060	6.88	5.19e–07	3.53	(2–1)		
13492−0325	5.00	–41.00	0.250	0.051	1.84	3.96e–07	3.98	(1–0)	Y	SiO overshoot,
–	4.50	–40.75	1.050	0.106	6.73	3.52e–07	3.88	(2–1)		see text and Fig. 18
14280−2952	6.00	–1.00	0.060	0.014	0.50	4.68e–07	4.07	(1–0)	–	
–	5.50	–1.50	0.250	0.070	2.06	4.24e–07	3.99	(2–1)		
15094−6953	10.00	–2.50	0.180	0.011	2.67	6.13e–07	8.69	(1–0)	–	
–	8.50	–2.00	0.560	0.076	7.51	4.29e–07	7.54	(2–1)		R
15223−0203	11.00	9.00	0.250	0.101	2.20	1.13e–06	5.33	(1–0)	N	2p, see text and Fig. 22
–	11.00	9.00	0.600	0.090	8.48	8.65e–07	4.57	(2–1)		2p
15410−0133	10.00	–1.00	0.100	0.053	0.89	6.25e–07	3.93	(1–0)	Y	marginal detection
–	10.00	–1.00	0.450	0.145	7.39	6.64e–07	4.07	(2–1)		R, SiO strongly variable
17102−1031	15.00	–28.00	0.110	0.010	2.22	2.37e–06	7.24	(1–0)	–	
–	12.00	–29.50	0.280	0.064	5.41	1.38e–06	5.79	(2–1)		
17265−0725	10.00	–8.50	0.500	0.088	7.19	1.47e–06	6.47	(1–0)	Y	R, SiO strongly variable
–	10.00	–8.00	1.100	0.080	16.85	1.08e–06	5.40	(2–1)		R, contam. by IS line
17398−4344	9.00	5.50	0.120	0.052	1.43	7.04e–07	4.39	(2–1)		noisy
17539+1037	12.00	–19.00	0.200	0.072	3.32	1.81e–06	6.78	(1–0)	Y	R
–	11.00	–18.50	0.530	0.077	8.81	1.30e–06	5.79	(2–1)		R, horns?
18243+0352	15.00	5.00	0.100	0.071	0.96	1.41e–06	5.35	(1–0)	Y	
–	12.00	2.00	0.420	0.191	6.98	1.06e–06	4.97	(2–1)		triangular
18359+0847	5.00	–55.00	0.350	0.125	2.07	2.52e–07	3.06	(1–0)	Y	marginal detection
–	6.00	–55.00	0.850	0.202	7.41	2.50e–07	2.83	(2–1)		SiO strong, overshoot
19143−5032	9.00	–32.50	0.140	0.016	1.65	1.22e–06	6.04	(1–0)	–	
–	8.00	–33.00	0.320	0.030	3.68	7.76e–07	4.87	(2–1)		R
19247−1722	10.00	–35.00	0.085	0.014	1.28	1.55e–06	6.65	(1–0)	–	R
–	9.00	–35.00	0.170	0.060	2.57	9.34e–07	5.18	(2–1)		R
19267+0345	13.00	1.00	0.100	0.049	1.33	1.92e–06	6.78	(1–0)	N	
–	13.00	1.00	0.250	0.063	3.86	1.50e–06	5.89	(2–1)		
19510−5919	9.00	–18.00	0.080	0.032	1.13	4.98e–07	3.59	(2–1)		
20120−4433	13.50	–31.00	0.420	0.020	8.31	4.85e–06	11.40	(1–0)	–	
–	9.00	–29.50	0.620	0.054	7.36	1.63e–06	7.14	(2–1)		P
20359−3806	10.00	–4.00	0.060	0.024	0.91	1.19e–06	5.71	(1–0)	–	
–	8.50	–5.00	0.210	0.052	2.53	8.88e–07	5.14	(2–1)		
20443+0215	3.50	–27.00	0.180	0.043	0.94	1.00e–07	2.07	(2–1)	Y	see text and Fig. 19
20479+0554	9.00	16.00	0.200	0.051	2.60	1.46e–06	6.71	(1–0)	Y	R
–	10.00	16.50	0.470	0.094	6.74	1.28e–06	5.96	(2–1)		R
20526−5431	8.50	29.50	0.080	0.011	1.03	2.16e–06	8.61	(1–0)	–	
–	7.00	30.00	0.320	0.064	3.35	1.65e–06	7.97	(2–1)		P
21044−1637	12.00	–3.00	0.065	0.011	1.13	1.08e–06	5.03	(1–0)	–	P
–	10.00	–3.00	0.260	0.062	3.75	8.45e–07	4.68	(2–1)		P
21197−6956	10.00	–4.50	0.130	0.019	1.75	4.00e–07	6.79	(1–0)	–	P
–	8.50	–3.50	0.360	0.030	4.31	2.65e–07	5.70	(2–1)		P
21368−3812	9.00	–29.00	0.035	0.016	0.47	9.44e–07	5.21	(1–0)	–	marginal detection
–	8.50	–27.00	0.220	0.028	2.78	1.10e–06	5.83	(2–1)		
21377−0200	6.00	–19.00	0.350	0.057	3.28	7.65e–07	5.42	(1–0)	Y	R
–	6.00	–19.00	1.180	0.086	10.21	7.00e–07	5.15	(2–1)		R
21439−0226	1.00	–34.00	1.850	0.078	2.38	4.74e–08	2.21	(1–0)	Y	D, see text and Fig. 11
–	11.00	–34.00	1.100	0.078	18.71	9.65e–07	4.87	(1–0)		
–	1.00	–34.00	7.670	0.317	10.22	4.83e–08	2.23	(2–1)		
–	11.00	–34.00	3.000	0.317	51.73	7.91e–07	4.34	(2–1)		
22142−8454	13.00	–1.00	0.050	0.016	0.59	8.82e–07	4.32	(1–0)	–	marginal detection
–	10.50	–2.50	0.100	0.026	1.52	4.60e–07	3.23	(2–1)		very noisy, LRS

Table 2. continued.

IRAS name	$v_{\rm exp}$ [km s^{-1}]	$v_{\rm lsr}$ [km s^{-1}]	$T_{\rm mb}$ [K]	rms [K]	$\int T_{\rm mb}\,{\rm d}v$ [K km s^{-1}]	$\dot{M}$ [$M_\odot$ yr^{-1}]	$R_{\rm CO}$ [10^{16} cm]	line CO	SiO	comments
22190−0751	7.00	15.00	0.350	0.098	3.86	6.23e–07	4.52	(1–0)	N	R
–	7.00	14.50	1.200	0.106	12.18	5.75e–07	4.32	(2–1)		P
22196−4612	15.00	–11.00	0.700	0.016	16.40	2.73e–06	7.85	(1–0)	–	2p, see text and
–	14.00	–12.00	2.200	0.104	46.63	2.19e–06	7.11	(2–1)		Knapp et al. (1999)
22540−5740	8.50	–39.50	0.040	0.010	0.43	4.12e–07	3.29	(1–0)	–	noisy
–	5.50	–39.50	0.180	0.018	1.05	2.41e–07	2.87	(2–1)		noisy, LRS
23041+1016	9.00	24.00	0.100	0.058	0.81	5.68e–07	3.88	(1–0)	Y	SiO overshoot,
–	5.50	24.00	0.770	0.102	5.83	4.06e–07	3.89	(2–1)		see Fig. 20
23134−7031	2.50	–20.50	0.054	0.012	0.15	8.07e–08	2.09	(2–1)	–	2 possib. lines, see Fig. 24
–	4.00	64.00	0.052	0.012	0.20	1.51e–07	2.48	(2–1)		⇒ both are not used here

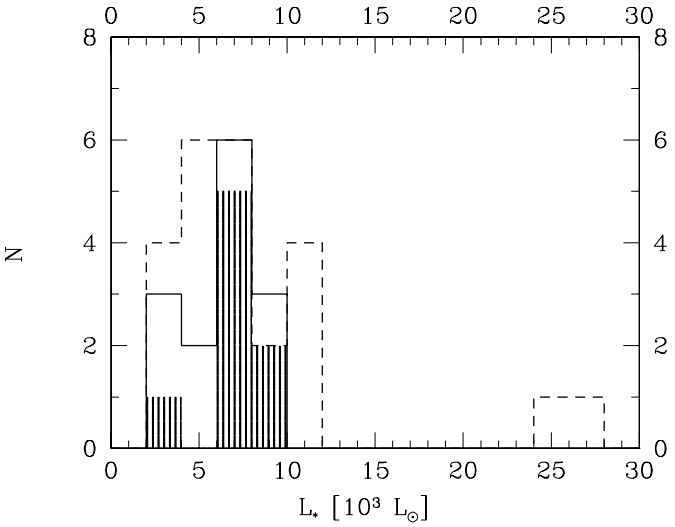

Fig. 1. Histogram of luminosities derived from the P-L relation (solid line, shaded areas: Miras, rest: SRb) and luminosities derived from the Hipparcos parallax (dashed line).

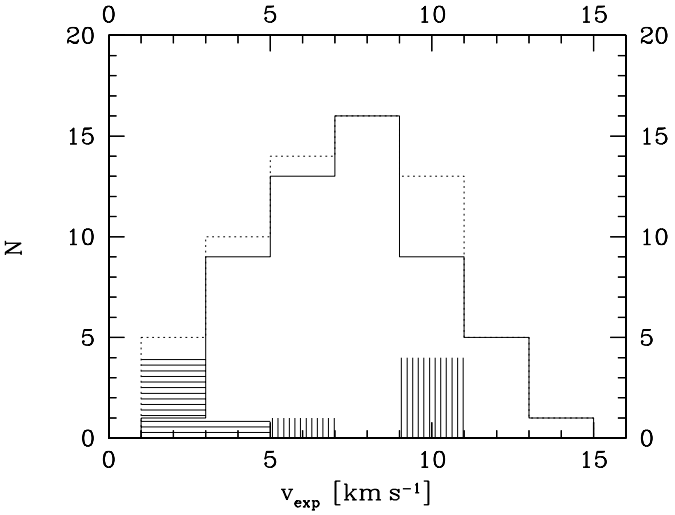

Fig. 2. Histogram of the expansion velocity distribution of our sample. Solid line: single winds only, dotted line: distribution including the double wind components; horizontal shading: narrow component, vertical shading: broad component (see text in Sect. 4.2).

The temperatures ($T_{\rm mb}$), velocities ($v_\star$ and $v_{\rm exp}$, determined at zero intensity level), the rms noise, as well as the integrated intensities derived from both, the CO(2–1) and (1–0) line, are listed in Table 2. The values given for the CO(2–1) line refer to the high resolution spectra whenever available, the exceptions are marked in the comments column of Table 2. The integrated intensities were determined by integrating the observed spectra in the range $[v_\star - v_{\rm exp}, v_\star + v_{\rm exp}]$.

Figure 2 displays a histogram of the velocity distribution (derived from the (2–1) lines) of our sample both, for the single winds only (solid line) and including all wind components (dashed line). About 45% of the single winds (54 sources) have velocities below 8 km s^{-1}, 10 single winds (19%) have $v_{\rm exp} \leq 5$ km s^{-1}, 33 sources (61%) have 5 km s^{-1} $< v_{\rm exp} \leq$ 10 km s^{-1}, and we have only 11 single-wind sources (20%) with $v_{\rm exp} \geq 10$ km s^{-1}. These numbers confirm, that the selection criteria used to set up our sample were appropriate for our purpose. The lowest values of $v_{\rm exp}$ are found from the narrow CO line components of EP Aqr, SV Psc, and o Cet, which indicate a velocity of only about 1.5 km s^{-1} (the broad component gives 7 km s^{-1} for o Cet and 11 km s^{-1} for EP Aqr and SV Psc).

4.3. Mass-loss rates

We use the expressions given by Loup et al. (1993) (scaled to the diameter of the telescope used) to evaluate both, the mass-loss rates and the CO photo-dissociation radii. This method is based on an approximate equation for the mass-loss rate, which represents the results obtained by Knapp & Morris (1985) for the CO(1–0) line and on the CO photo-dissociation radii derived by Mamon et al. (1988). Unfortunately, no equivalent representation for the mass-loss rate has been published so far for the CO(2–1) transition. Therefore, we re-scale the Knapp & Morris expression by a factor $\langle\, T_{\rm mb}^{(2-1)} \,/\, T_{\rm mb}^{(1-0)} \,\rangle$, which accounts for the average ratio of the peak main-beam brightness temperatures of the (2–1) and (1–0) line (see, e.g., Olofsson et al. 1993). Thus, we are using our (1–0) spectra only (if (2–1) data have been obtained), to determine the average peak-intensity ratio. In our sample observed with the SEST, we have 19 sources with (1–0) and (2–1) profiles. (The 20th. source, R Hya, which has a composite (2–1) profile is excluded here, since the resolution of the (1–0) line doesn't allow to

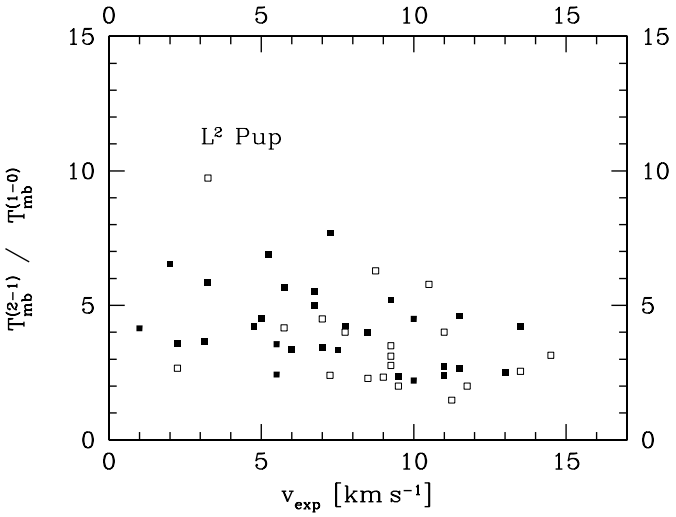

Fig. 3. Ratio of the peak main-beam brightness temperature in the CO(2–1) and CO(1–0) lines vs. outflow velocity. Filled squares: IRAM, open squares: SEST.

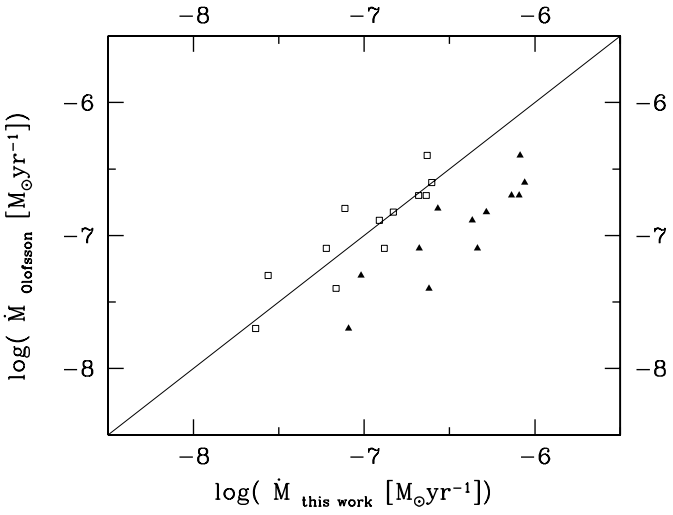

Fig. 4. Mass-loss rates derived by Schöier & Olofsson (2001) and Olofsson et al. (2002), respectively, vs. mass-loss rates derived in this work (assuming the same distance as in their work) for the 12 (single wind) objects in common to our samples (filled triangles). The open squares represent our mass-loss estimates divided by a factor 3.5.

decompose the profile into 2 components.) The 19 sources are plotted as open squares in Fig. 3, the outstanding object is L^2 Pup. For these 19 sources, the average peak main-beam brightness temperature ratio is $T_{\rm mb}^{(2-1)}$ / $T_{\rm mb}^{(1-0)}$ = 3.62 ± 1.95. If we exclude L^2 Pup, we get an average peak main-beam brightness temperature ratio of 3.28 ± 1.27, i.e. a strongly reduced standard deviation. At IRAM, we got 31 sources with (1–0) and (2–1) profiles (filled squares in Fig. 3), their average intensity ratio is $T_{\rm mb}^{(2-1)}$ / $T_{\rm mb}^{(1-0)}$ = 3.97 ± 1.27. The mean value of the intensity ratio between IRAM and SEST observations, weighted by the respective number of sources, is 3.84 ± 1.53. If we exclude L^2 Pup, the weighted mean is 3.72 ± 1.27. To re-scale the Knapp & Morris expression, we therefore use an intensity ratio of 4 for all sources. We checked, that there is no trend of the intensity ratio with outflow velocity (see Fig. 3).

To convert the CO mass-loss rates to gas (hydrogen) mass-loss rates, we assume a CO/H_2 ratio of 2×10^{-4} for M- and S-stars (Olofsson et al. 2002) and 1×10^{-3} for C-stars (Schöier & Olofsson 2001). The resulting mass-loss rates and CO dissociation radii are listed in Table 2 both, for the CO(2–1) and (1–0) lines.

4.4. Discussion of the derived mass-loss rates and expansion velocities

Recently, Olofsson and co-workers have investigated the mass-loss properties of a sample of bright carbon stars (Schöier & Olofsson 2001) and irregular and semiregular M-type variables (Olofsson et al. 2002) on the basis of a radiative transfer model for the circumstellar CO radio line emission. In order to derive the mass-loss rate of an individual object, they take into account several CO transitions (if available, (1–0), (2–1), (3–2), and (4–3)) and minimize the deviation between the velocity integrated line intensity in the model profiles and in the observed profiles. They conclude, that their detailed modeling results in mass-loss rates which are on average ten times higher than the mass-loss rates derived from the Knapp & Morris (1985) and the Kastner (1992) expressions, at least for the low mass-loss rate objects in their sample.

In Fig. 4 we present a comparison between the mass-loss rates derived in this work from the (2–1) line with the mass-loss rates derived by Schöier & Olofsson (2001) and Olofsson et al. (2002) for the 12 (single wind) objects in common to our samples. For this comparison, we used their distances to calculate the mass-loss rates by the Loup et al. (1993) method applied in the present work. From Fig. 4 it can be seen, that the mass-loss rates derived here (assuming the same distances) are systematically higher than the Olofsson et al. estimate by an average factor 3.5 ± 1.4. There is no discernible trend with mass-loss rate, at least not in the range of mass-loss rates relevant for the present work.

Another difference found between our work and that of Olofsson et al. concerns the derived expansion velocities. We determine the velocity by simply fitting a parabola to the line profile, whereas Olofsson et al. derive it from the model fits, including the effect of turbulent line broadening by an assumed constant turbulence velocity of 0.5 km s^{-1}. The velocities reported here agree well with those of Kerschbaum & Olofsson (1999) (who use the same method as we do), but are on average higher by 0.84 km s^{-1} than those derived by Schöier & Olofsson (2001) and Olofsson et al. (2002). This seems to be a constant offset, independent of the velocity itself (see Fig. 5; there are only 11 data points, because the 2 C-rich objects, X TrA and Y Pav, have the same velocity of 8 km s^{-1} (Schöier & Olofsson 2001) and 8.5 km s^{-1} (present work), respectively).

The model of Schöier & Olofsson (2001) and Olofsson et al. (2002) makes however some standard assumptions, like a constant mass-loss rate and a constant turbulence velocity, which may not be justified. Kemper (2002) demonstrates, that including even higher CO transitions than (4–3) (they use lines up to (7–6)) leads to the conclusion of either temporal mass-loss variations by factors of 2 to 10 on time scales of a few

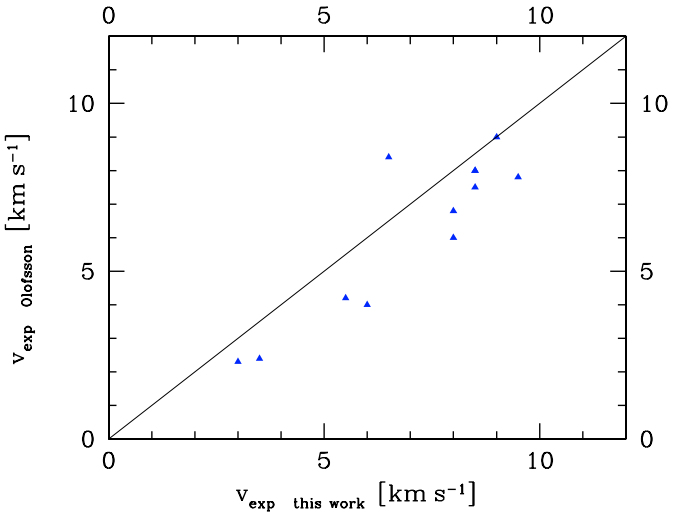

Fig. 5. Gas expansion velocities derived by Schöier & Olofsson (2001) and Olofsson et al. (2002), respectively, vs. those derived in the present work for the 12 (single wind) objects in common to our samples (filled triangles).

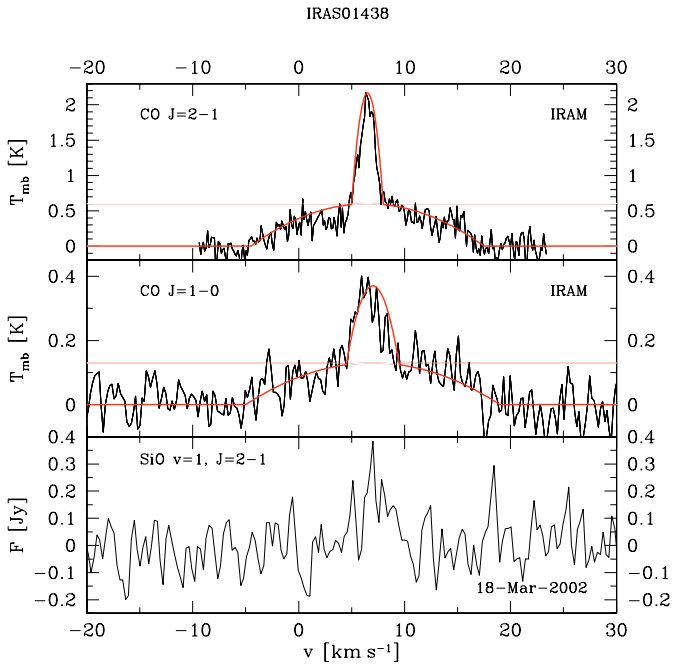

Fig. 6. High-resolution CO(2–1) line profile (upper panel), CO(1–0) line profile (middle panel), and SiO maser line at 86 GHz (lower panel) of SV Psc. Also shown is a fit to the CO profiles, assuming two independent wind components. Note, that the SiO line suggests larger velocities than the narrow CO component.

hundred to a thousand years or of a non-constant turbulence velocity, or both of these effects. Kemper (2002) also demonstrates, that the value assumed for the (constant) turbulence velocity strongly affects the calculated main-beam brightness temperature (see her Fig. 7.8) and thus the integrated line intensity.

Given this intricate situation, we will keep here to our simple approach to derive mass-loss rates and gas expansion velocities and note, that our mass-loss rates can be scaled to the ones found by Olofsson et al. by dividing them by a factor 3.5 (for the same distance, of course) and that our outflow velocities are on average higher by 0.84 km s^{-1} than the ones found by Olofsson et al. (2002). As these differences are systematic, the comparison with our models should be performed at a qualitative level. This situation will stay as long as there is no convergence on a unique and reliable method to derive mass loss rates from CO rotational line profiles.

4.5. Non-standard line profiles

4.5.1. Composite profiles

In our sample, we have 5 objects which clearly show composite CO profiles, i.e. a narrow component is superimposed on a broader one while both components are centered on the same stellar velocity. This type of profiles has been discussed extensively by Knapp et al. (1998) who interpret them in terms of two successive winds with different mass-loss rates and outflow velocities, emanating from the same star. Another scenario to explain narrow CO profiles has been pushed forward in a series of papers by Jura and Kahane and is summarized in Jura & Kahane (1999). For four objects (Red Rectangle, BM Gem, EU And, and AC Her) they find narrow CO profiles (*FWHM* $<$ 2.5 km s^{-1}) which they interpret in terms of molecular gas orbiting the star in a circumstellar disk in Keplerian rotation. While this scenario seems plausible for cases with a very narrow component (*FWHM* $\approx$ 2 km s^{-1}) (e.g., Red Rectangle, BM Gem), it seems questionable, whether it also applies to sources where the narrow component indicates a velocity of several km s^{-1}. In one case, X Her, Kahane & Jura (1996) find a composite CO profile, where the narrow component indicates a velocity of 2.5 km s^{-1} and the broad one a velocity of 10 km s^{-1}. In this case, the intensity contours of the blue and red wings of the "high-velocity" component are symmetrically displaced from the peak position of the slow component. Kahane & Jura (1996) interpret this observation in terms of a slow, spherical wind responsible for the narrow line component and a non-spherical ("bipolar") outflow which produces the broad component of the line profile. In the following, we will adopt the double-wind interpretation of Knapp et al. (1998) and give some support to this interpretation based on our model calculations (see also Sect. 5); of course, this interpretation does not preclude that one or both winds may show moderate deviations from spherical symmetry.

IRAS 01438+1850 (≡SV Psc): CO(2–1) observations of this source have previously been presented by Kerschbaum & Olofsson (1999) whereas Kerschbaum et al. (1996) did not detect the CO(1–0) line in this source. In Fig. 6 we present our observations in the CO(2–1) and (1–0) lines and in the SiO 86 GHz maser. Both, in the CO(1–0) and (2–1) lines we find clear composite profiles, indicating velocities of about 2 km s^{-1} and 11 km s^{-1}, respectively, and yielding mass-loss rates of 1×10^{-7} $M_\odot$ yr^{-1} and 1×10^{-6} $M_\odot$ yr^{-1} (cf. Table 2), typical of our B-type and A-type models. The SiO maser in SV Psc is time variable (on December 2, 2001

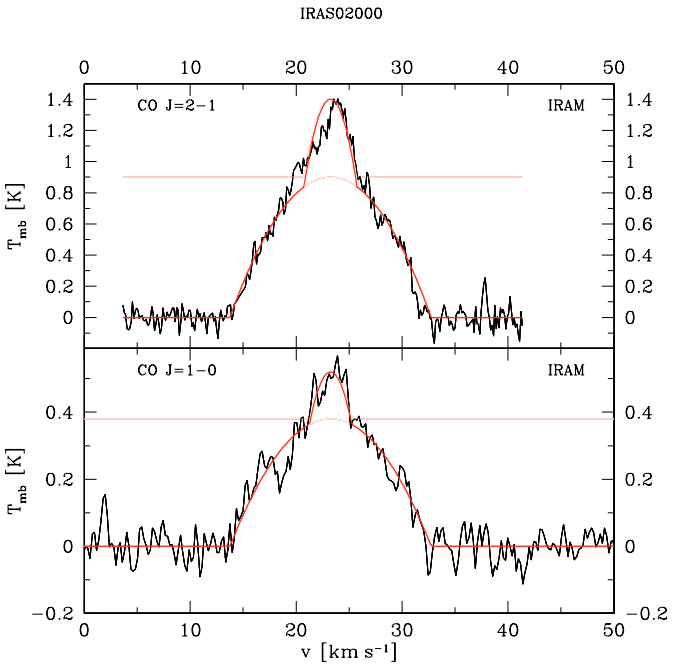

Fig. 7. High-resolution CO(2–1) profile (upper panel) and CO(1–0) profile (lower panel) of RAFGL 292. Also shown is a fit to both profiles, assuming two wind components.

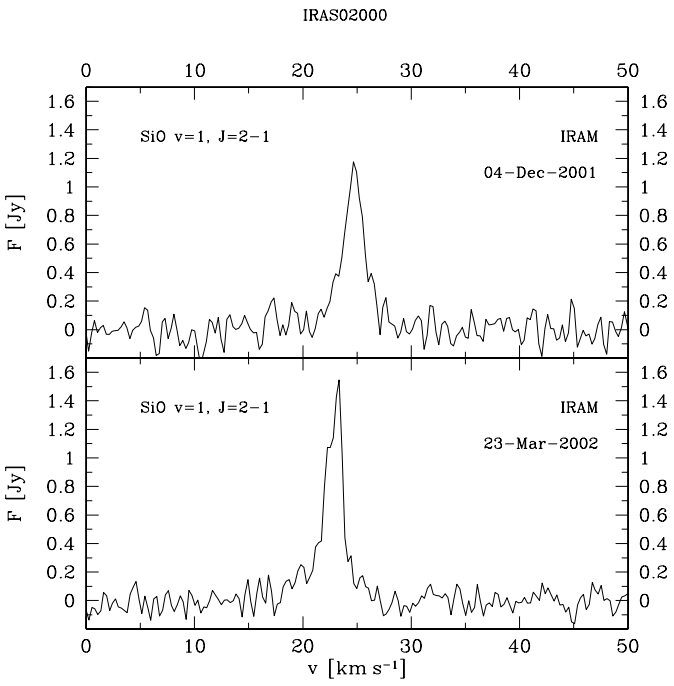

Fig. 8. SiO 86 GHz profiles of RAFGL 292 at two epochs. Note, that the SiO maser indicates higher velocities than those derived from the narrow component of the CO line profiles.

we only had a tentative detection) and it suggests velocities of (at least) $\pm 5\,\mathrm{km\,s^{-1}}$ w.r.t. the star, significantly higher than the velocity of the narrow CO components.

IRAS 02000+0726 (≡RAFGL 292) was detected here for the first time in CO and in the SiO 86 GHz line. It shows a triangular profile both, in the CO(2–1) and (1–0) line (Fig. 7).

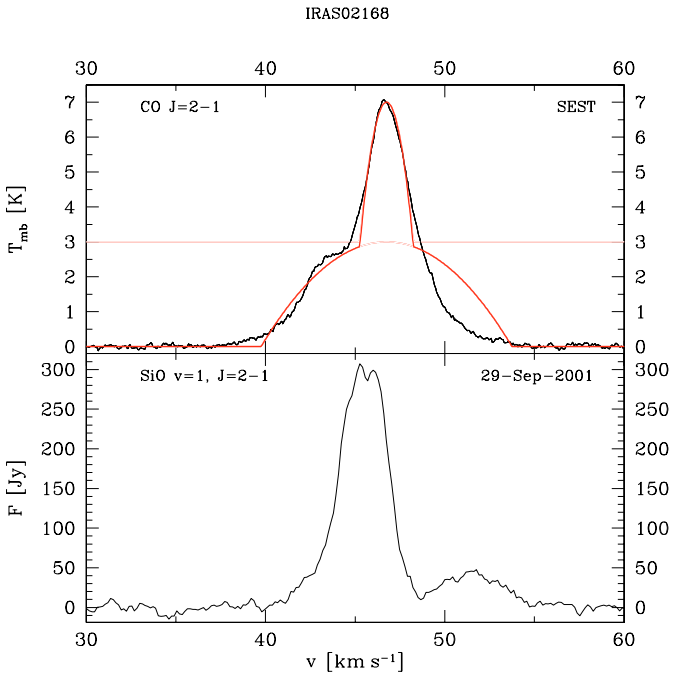

Fig. 9. High-resolution CO(2–1) profile (upper panel) and SiO 86 GHz profile (lower panel) of o Cet. Also shown is a fit to the CO profile, assuming two independent wind components. The SiO maser indicates higher velocities than those derived from the broad CO line profile.

Knapp et al. (1998) demonstrate, that such triangular profiles can be the result of two successive spherical winds which are expanding at different velocities (see their Fig. 2.a). Adopting the same interpretation for our CO observations of RAFGL 292, we fitted two independent parabolas to each, the CO(2–1) and (1–0) profiles, see Fig. 7. The resulting values for the outflow velocities and mass-loss rates for both wind components are listed in Table 2. The derived properties for both winds are again typical for our B-type and A-type models, respectively.

The triangular shape of the measured profile is similar to the one of IRC +60144 (a carbon star) which has been obtained by Knapp et al. (1998) and interpreted as a double wind. However, that profile is about a factor 2 wider in both components ($v_{\mathrm{broad}} = 20.5\,\mathrm{km\,s^{-1}}$, $v_{\mathrm{narrow}} = 5.6\,\mathrm{km\,s^{-1}}$) than the profile of RAFGL 292. In Fig. 8, the SiO 86 GHz maser is shown for the two epochs of our observations of this star, showing clear time variability. Also, the maser line indicates higher velocities than those derived from the narrow CO components, a configuration reminiscent of L^2 Pup (see Winters et al. 2002).

IRAS 02168−0312 (≡Mira ≡ o Cet): An asymmetric composite profile of the CO(3–2) line with a strong blue shifted emission component has previously been presented by Knapp et al. (1998), who interpret it in terms of double winds. In Fig. 9 we present our observations of the CO(2–1) line and of the SiO 86 GHz profile. A clear asymmetry of the CO profile can be seen, with a pronounced bump to the left of the stellar velocity. This shape is very similar to the (3–2) profile displayed in Knapp et al. (1998). Superposed on our CO(2–1) observation is a fit to the profile assuming two wind components, the

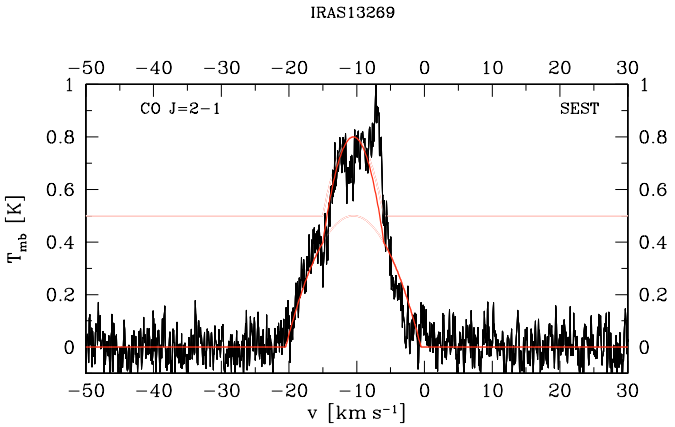

Fig. 10. High-resolution CO(2–1) profile of R Hya. Also shown is a fit to the profile, assuming two independent wind components.

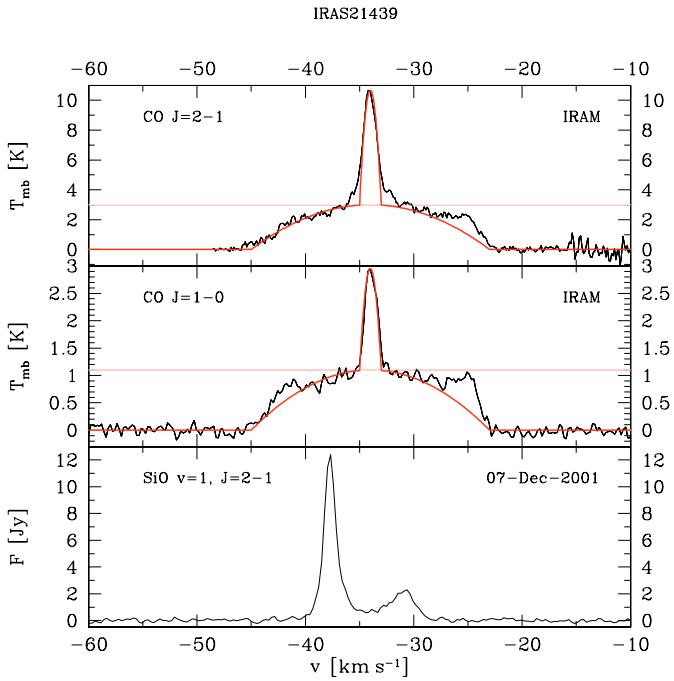

Fig. 11. High-resolution CO(2–1) line profile (upper panel), CO(1–0) profile (middle panel), and SiO maser line at 86 GHz (lower panel) of EP Aqr. Also shown is a fit to the CO profiles, assuming two wind components. Note, that the SiO line indicates larger velocities than the narrow CO component.

respective outflow velocities and mass-loss rates are listed in Table 2. The SiO maser line shown in the lower panel of Fig. 9 indicates a maximum velocity of about 8 km s^{-1} w.r.t. the star, higher than the outflow velocity of 7 km s^{-1} derived for the broad CO component. From detailed Monte-Carlo radiative transfer calculations, Ryde & Schöier (2001) find that the asymmetric shape of the CO rotational lines can be reasonably well explained by self-absorption in a single, spherically symmetric wind with constant mass-loss rate and a turbulent velocity of $v_t = 1.5$ km s^{-1}. However, to model the low excitation ro-vibrational infrared lines in the CO fundamental band, they are led to invoke an inner cavity of the circumstellar shell, devoid of CO, which extends out to 2.5×10^{15} cm (corresponding to 53 stellar radii). Several reasons for the existence of such a cavity are proposed by Ryde & Schöier, one of them being a reduction of the mass-loss rate and outflow velocity, resembling the double wind interpretation by Knapp et al. (1998). Nevertheless, the values for the properties of the two winds derived here from our simple, symmetric, two-component parabolic fit to the asymmetric profile of o Cet should be handled with care. A different interpretation for the asymmetric line profile has been proposed by Josselin et al. (2000), who argue on the basis of CO(2–1) mapping observations and KI long-slit spectroscopy for a spherical envelope which is disrupted by a slow bipolar outflow.

IRAS 13269−2301 (≡R Hya) also shows an asymmetric CO(2–1) profile (see Fig. 10) with a blue-shifted emission component, very similar to the CO(3–2) profile presented by Knapp et al. (1998). They interpret the profile in terms of a double wind and derive velocities of $v_{\rm narrow} = 5$ km s^{-1}, $v_{\rm broad} = 11$ km s^{-1} and mass-loss rates of $\dot{M}_{\rm narrow} = 7.3 \times 10^{-8}\ M_\odot$ yr^{-1} and $\dot{M}_{\rm broad} = 4.7 \times 10^{-7}\ M_\odot$ yr^{-1}. The corresponding results of our fit are listed in Table 2 and are in good agreement with the Knapp et al. values (if we assume their distance of 200 pc and their CO/H$_2$ ratio of 5×10^{-4}, we get $\dot{M}_{\rm narrow} = 9.9 \times 10^{-8}\ M_\odot$ yr^{-1} and $\dot{M}_{\rm broad} = 3.9 \times 10^{-7}\ M_\odot$ yr^{-1}). The interpretation of the CO line profiles in terms of a double wind for this source seems to be supported by spatially resolved IRAS observations presented and discussed in Hashimoto et al. (1998). They find indications for a detached circumstellar dust envelope around R Hya, with a radius of about 3 arcmin. According to their analysis, the mass-loss rate of R Hya has dropped about a hundred years ago, suggesting that R Hya experienced already at least one major variation in its mass-loss. The 2 winds suggested by the CO line profiles however, should both reside inside the detached shell detected by Hashimoto et al. (1998) since the CO photo-dissociation radius derived here (see Table 2) would correspond to only about 18 arcsec at a distance of 125 pc. R Hya may therefore represent a case similar to RS Cnc, for which the IRAS data indicate an excess at 60 μm ascribed to a detached shell (Young et al. 1993a) while the CO lines (Knapp et al. 1998) and the HI line (Gérard & Le Bertre 2003) indicate 2 winds.

IRAS 21439−0226 (≡EP Aqr) shows a rather symmetric composite profile in the CO(1–0) and (2–1) lines (see Fig. 11) as well as in the (3–2) line (see Knapp et al. 1998). It also shows a strong SiO maser which indicates velocities in excess of the velocity traced by the narrow CO component. The 86 GHz SiO maser has been detected by Haikala et al. (1994), although with a much lower S/N ratio. Composite CO(3–2) and (2–1) profiles were presented by Knapp et al. (1998) who derive velocities $v_{\rm narrow} = 1.4$ km s^{-1}, $v_{\rm broad} = 10.8$ km s^{-1} and mass-loss rates of $\dot{M}_{\rm broad} = 2.3 \times 10^{-7}\ M_\odot$ yr^{-1} and $\dot{M}_{\rm narrow} = 1.7 \times 10^{-8}\ M_\odot$ yr^{-1}. A composite CO(1–0) profile was previously presented by Margulis et al. (1990) and later by Kerschbaum & Olofsson (1999). This source was found to be extended from IRAS data (Young et al. 1993b), indicating some

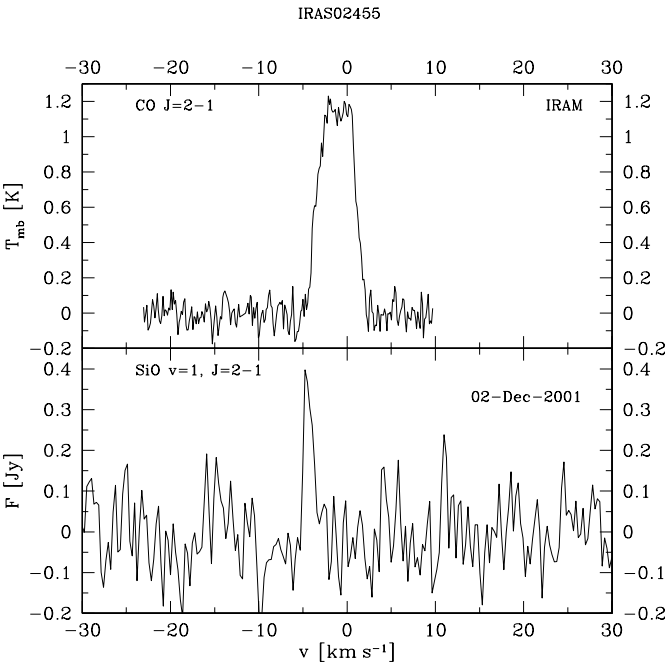

Fig. 12. High-resolution CO(2–1) profile (upper panel) and SiO 86 GHz profile (lower panel) of T Ari. Note, that the SiO maser indicates higher velocities than those derived from the CO line profile.

major variation in mass-loss some 5000 yr ago which, as in the case of R Hya, seems to support the double wind interpretation of the CO line profiles.

4.5.2. Narrow profiles

We have in our sample 10 objects, whose (one component) CO line profiles indicate wind velocities $v_{\rm exp} \leq 5\,{\rm km\,s^{-1}}$. Since these objects are of particular relevance for us in the context of our low mass-loss rate models, all of them will be addressed in this section.

IRAS 02455+1718 (≡T Ari): This source shows narrow, rectangular CO profiles (see Fig. 12, a (2–1) profile obtained with the SEST is shown in Kerschbaum & Olofsson 1999). T Ari is a semiregular variable of type SRa, for which a uniform-disk diameter of $\Phi_{\rm UD} = 7.08 \pm 0.13$ mas and a stellar temperature of $T_{\rm eff} = 3080 \pm 45$ K has been determined from lunar occultation and from infrared photometry (yielding a bolometric flux of $1.579 \times 10^{-6}\,{\rm erg\,cm^2\,s^{-1}}$) (Richichi et al. 1999). Combining this with the measured Hipparcos parallax, we find a linear stellar radius of 1.71×10^{13} cm and a luminosity of $5120\,L_\odot$, in reasonable agreement with the luminosity derived by the bolometric correction (see Table 1). The outflow velocity and mass-loss rate derived from the CO line profiles (see Table 2) are in good agreement with our low mass-loss rate B-type models. The SiO maser indicates photospheric velocities in excess of the terminal wind speed as derived from the CO profiles, again in good agreement with the hydrodynamic structure of the B-type models (see also Sect. 5).

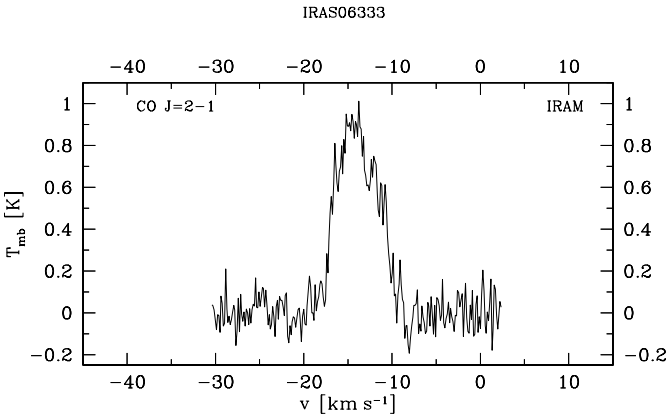

Fig. 13. High-resolution CO(2–1) profile of GL Mon.

IRAS 06333−0520 (≡GL Mon): We obtained a narrow CO(2–1) profile (see Fig. 13), whereas neither CO(1–0) nor the SiO 86 GHz maser were detected. The outflow velocity and mass-loss rate derived from the CO(2–1) profile fit well the properties of the B-type models. Our observation is probably a first detection, Kerschbaum & Olofsson (1999) did not detect this source in CO with the SEST.

IRAS 07120−4433 (≡L^2 Pup): Our observations of this source were already discussed in detail in Winters et al. (2002). It shows narrow CO(2–1) and (1–0) line profiles indicating an outflow velocity of the material in the circumstellar shell of only about $3\,{\rm km\,s^{-1}}$ and a broad SiO maser feature at 86 GHz, indicating an outward velocity of the material close to the stellar photosphere of at least $10\,{\rm km\,s^{-1}}$. This led us to consider L^2 Pup as a prototype for our B-type models, a conclusion reached independently by Jura et al. (2002). Very recently, González Delgado et al. (2003) presented thermal SiO($J = 2-1$) and (3–2) line profiles for this source. The width of the dominating line component agrees well with that of the CO lines, but the thermal SiO lines (notably the (3–2) line) also show extended line wings, indicating velocities up to $\sim 5\,{\rm km\,s^{-1}}$, intermediate between the CO and SiO-maser velocities. This would be in agreement with our B-type models, if the wings of the thermal SiO lines are formed in the transition region between the outer atmosphere and the inner circumstellar shell which, in the models, is located at around 2−3 stellar radii.

IRAS 07299+0825 (≡S CMi) shows narrow CO lines and a strong and broad SiO maser (see Fig. 14), indicating velocities in excess of the terminal outflow velocity probed by the CO lines. This is similar to the case of L^2 Pup, although the velocity difference is much less spectacular here. SiO velocities higher than the CO velocities for this source have already been noted by Cernicharo et al. (1997) and Herpin et al (1998), see Sect. 4.5.4. The wind properties derived here for S CMi (see Table 2) are in good agreement with the characteristics of our B-type models.

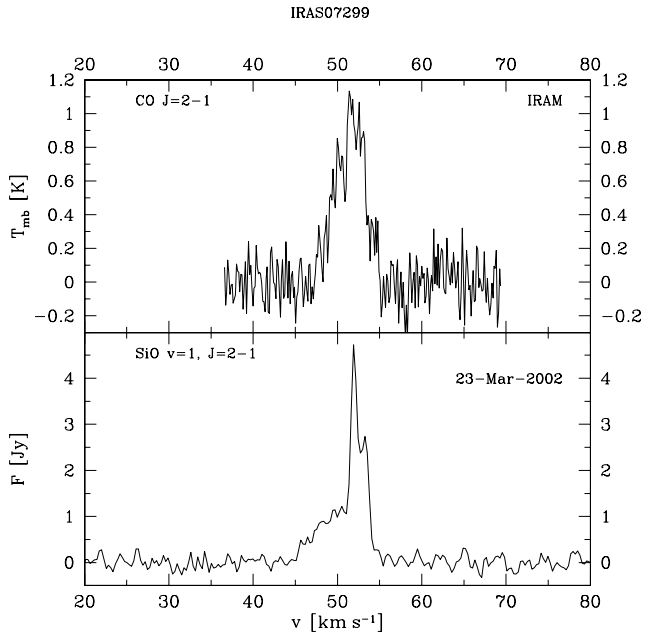

Fig. 14. High-resolution CO(2–1) profile (upper panel) and SiO 86 GHz profile (lower panel) of S CMi. Note, that the SiO maser indicates higher velocities than those derived from the CO line profile.

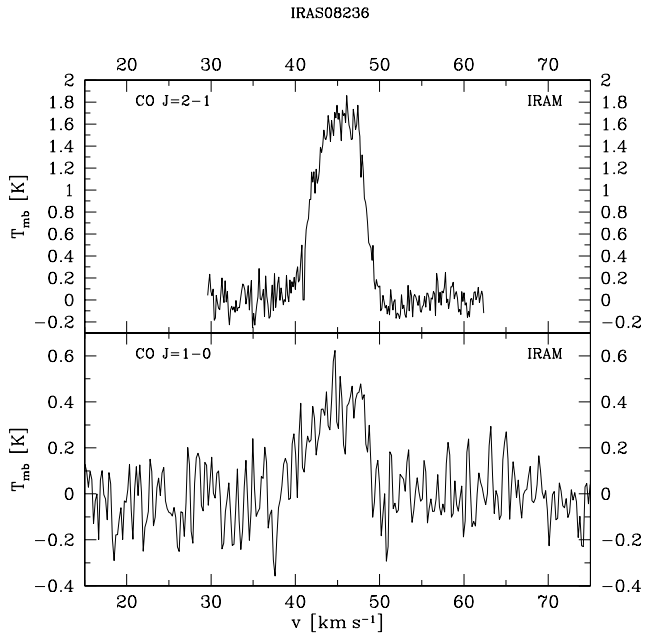

Fig. 15. High-resolution CO(2–1) profile (upper panel) and CO(1–0) profile (lower panel) of IRAS 08236−0444.

IRAS 08236−0444 is detected here for the first time in CO. The profiles indicate an outflow velocity of about 5 km s^{-1} (see Fig. 15 and Table 2) and the derived mass-loss rate would place it in the border region between A-type and B-type models. From our data, one could speculate that a SiO maser is also present, but this needs to be confirmed by further observations.

IRAS 08272−0609 (≡RT Hya) exhibits a strong, time variable SiO maser and a narrow, rectangular CO(2–1) profile (see Fig. 16). At least in our first observation, the velocity

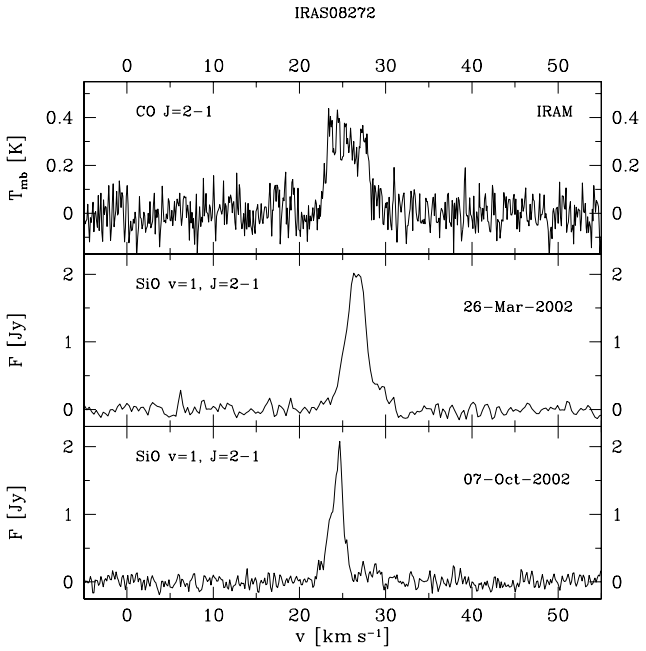

Fig. 16. High-resolution CO(2–1) line profile (upper panel, smoothed to a resolution of 80 kHz) and SiO maser line at 86 GHz (2nd and 3rd panel, observed six months apart) of RT Hya. The SiO maser line is time variable. At the first epoch, it indicates larger velocities than the CO line.

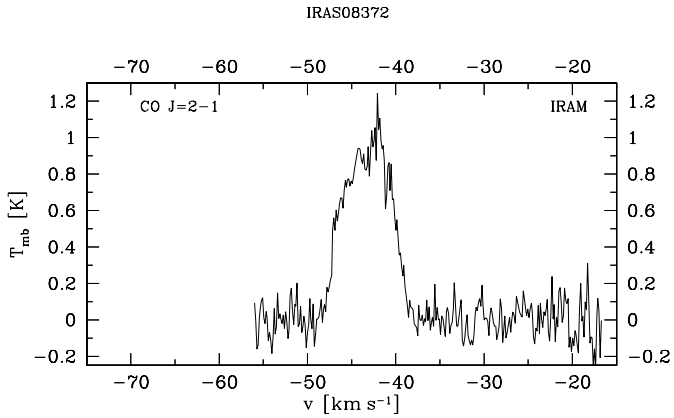

Fig. 17. High-resolution CO(2–1) profile of RV Hya.

indicated by the SiO maser exceeds the CO velocity. We did not detect the CO(1–0) line. The wind properties derived here (see Table 2) correspond to the B-type models. To our knowledge, this source is here detected for the first time in CO and in the SiO maser; it was searched for but not detected at 86 GHz (Patel et al. 1992) at a noise level of 4.8 Jy nor at 43 GHz (Hall et al. 1990) with a sensitivity of 6.3 Jy.

IRAS 08372−0924 (≡RV Hya) was detected here, to our knowledge, for the first time in CO(2–1) where it shows a narrow profile (see Fig. 17). We did neither detect it in CO(1–0) at a noise level of 0.065 K ($T_{\rm mb}$) nor in the 86 GHz SiO maser line at an rms noise of 0.098 Jy.

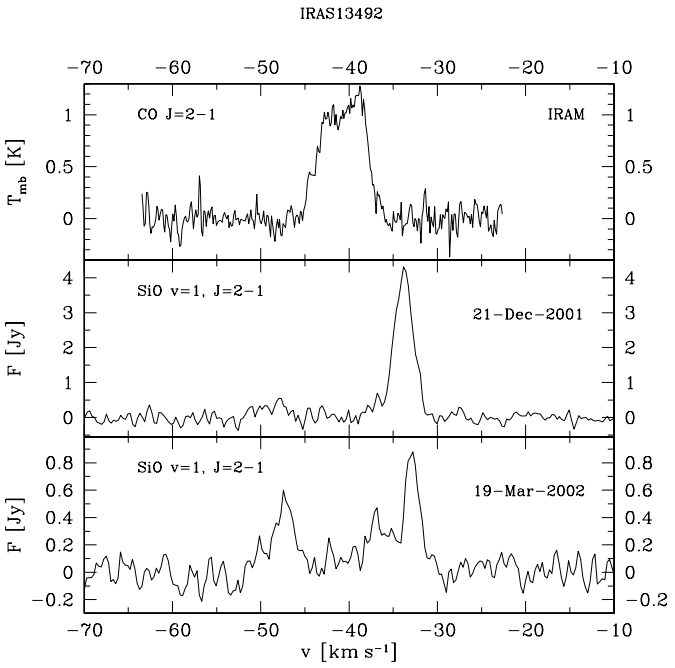

Fig. 18. High-resolution CO(2–1) line profile (upper panel) and SiO maser line at 86 GHz (2nd and 3rd panel, observed three months apart) of AY Vir. The SiO maser line is highly time variable (note the different scaling at both epochs). At both phases, it indicates much larger velocities than the CO line.

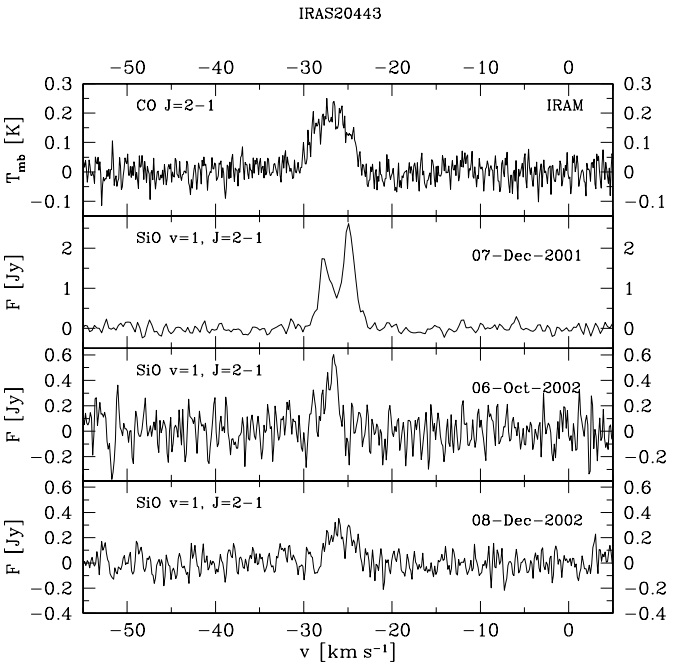

Fig. 19. High-resolution CO(2–1) line profile (smoothed to a resolution of 80 kHz, upper panel) and SiO maser line at 86 GHz (2nd, 3rd and last panel, observed at different epochs) of V Aqr. The SiO maser line is highly time variable (note the different scaling).

IRAS 13492–0325 (≡AY Vir) shows a rather narrow CO profile and a broad SiO maser line (see Fig. 18), indicating that the material close to the star moves at much higher velocity ($\approx$10 km s^{-1}) than the material in the circumstellar shell ($\approx$4.5 km s^{-1}). This velocity structure appears to be very similar to the one found in L^2 Pup (Winters et al. 2002). Both sources are of type SRb and both have similar periods. Also in both sources the SiO maser is highly time variable (cf. 2nd and 3rd panel in Fig. 18). From the CO line we estimate the mass-loss rate to $\sim 3.5 \times 10^{-7}$ $M_\odot$ yr^{-1} (cf. Table 2). A 22 GHz H_2O maser line was detected by Crocker & Hagen (1983), indicating a velocity of about 3 km s^{-1}. Engels et al. (1988) found a secondary feature in the line profile, suggesting that the H_2O maser in this source shows some time variability. Both, the velocity structure as probed by the SiO 86 GHz maser, the 22 GHz H_2O maser and the CO rotational lines and the mass-loss rate are in agreement with the properties of our B-type models (see also Sect. 5).

IRAS 20443+0215 (≡V Aqr) shows a narrow CO(2–1) profile (we did not detect this source in the (1–0) line) and a strongly variable SiO maser, see Fig. 19. Our CO and SiO observations seem to be first detections in this source. The wind properties derived from the CO profile (see Table 2) agree well with those expected from our low mass-loss rate (B-type) models.

IRAS 23041+1016 (≡R Peg) displays a narrow, rectangular CO(2–1) profile, see Fig. 20. We also obtained a rather noisy 115 GHz spectrum in which we tentatively identify the presence of a CO(1–0) line. R Peg has a strong SiO maser which indicates photospheric velocities in excess of the outflow velocity derived from the CO profile. The wind properties derived from the (2–1) line would correspond to an A-type model close to the border of the B-regime.

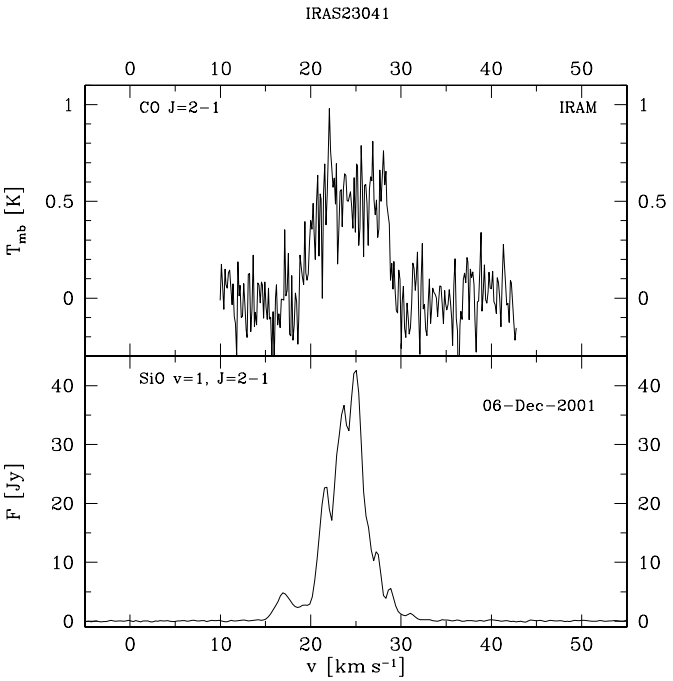

Fig. 20. High-resolution CO(2–1) line profile (upper panel) and SiO maser line at 86 GHz (lower panel) of R Peg. The SiO maser line indicates larger velocities than the CO line.

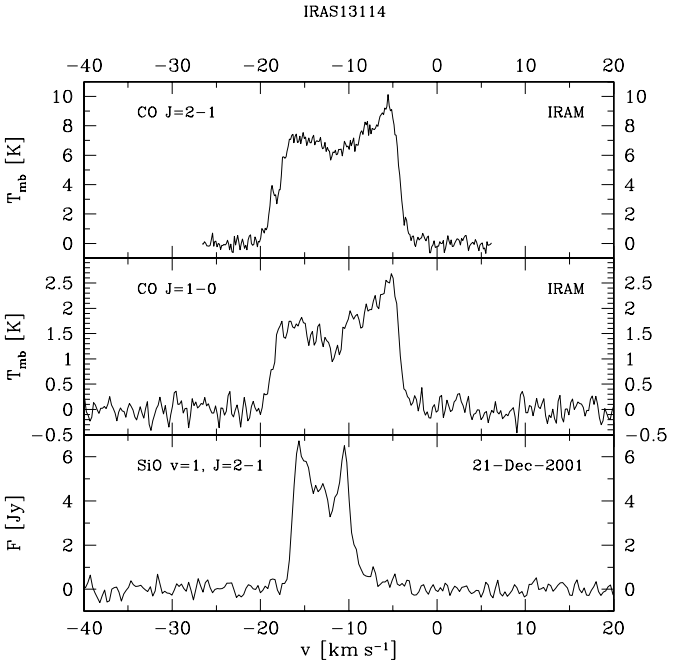

Fig. 21. High-resolution CO(2–1) line profile (upper panel), CO(1–0) profile (middle panel), and SiO maser line at 86 GHz (lower panel) of SW Vir.

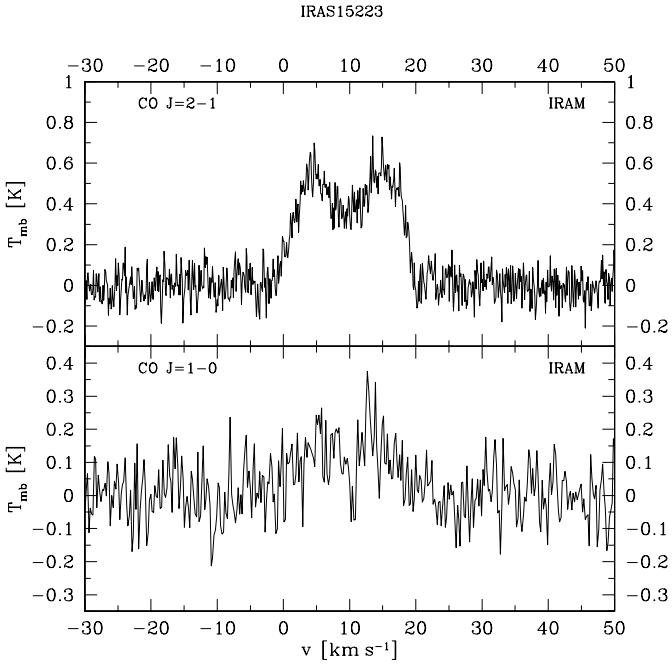

Fig. 22. High-resolution CO(2–1) profile (upper panel) and CO(1–0) profile (lower panel) of OV Ser. Both profiles are smoothed to a resolution of 80 kHz.

4.5.3. Other types

IRAS 13114−0232 (≡SW Vir): Our observations of the CO(2–1), (1–0), and of the SiO 86 GHz maser are shown in Fig. 21. The CO profiles display an asymmetric double-peaked shape with enhanced red-shifted emission. This line shape has been well fit by Kahane & Jura (1994) with a spherical model and assuming a micro-turbulence velocity of $2\,\mathrm{km\,s^{-1}}$. The asymmetry with reduced emission in the blue wing of the profile can be explained by self-absorption (see Nguyen-Q-Rieu et al. 1984; Morris et al. 1985). The wind properties derived here for this source are typical of an A-type model.

IRAS 15223–0203 (≡OV Ser) was detected here for the first time in CO. The spectra display double-peaked CO profiles, which in this source are rather symmetric (Fig. 22). We did not detect an 86 GHz SiO maser. The wind properties derived here correspond to those of our A-type models.

IRAS 22196–4612 (≡π^1 Gru): Our observations of this source are presented in Fig. 23. The profiles show an asymmetric, double-peaked structure and extended emission wings. Mapping data in CO(2–1) and (1–0) as well as a ^{13}CO(1–0) profile have already been presented and discussed by Sahai (1992). He interprets these observations in terms of a fast bipolar outflow oriented perpendicular to a dense equatorial disk, embedded in a slow, extended outflow. Later, this object has been re-discussed by Knapp et al. (1999) on the basis of CO(2–1) and SiO(6–5) data. From a broad-band CO(2–1) profile they find velocities up to $\approx$90 km s^{-1} w.r.t. the star whereas the SiO profile is fit by a parabola, resulting in an outflow velocity of $13\,\mathrm{km\,s^{-1}}$. From a CO(2–1) map covering ±50″ in right ascension and declination around the star they find, that

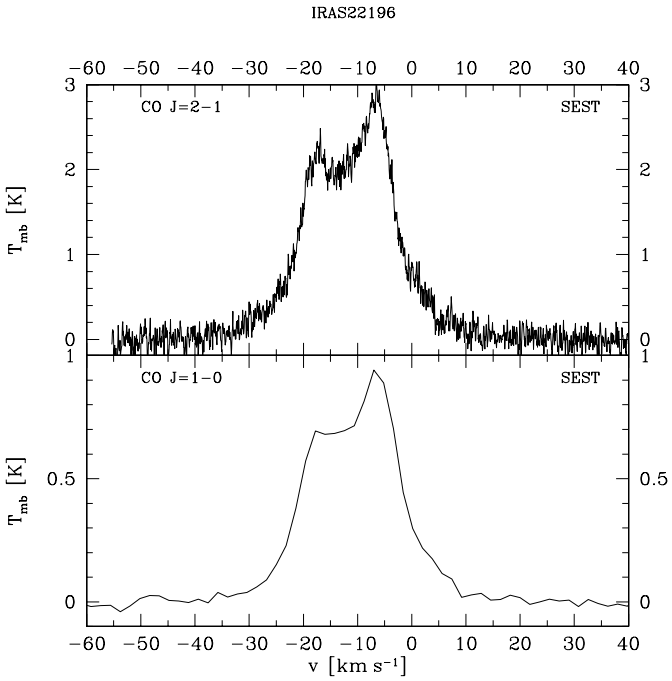

Fig. 23. High-resolution CO(2–1) profile (upper panel) and CO(1–0) profile (lower panel) of π^1 Gru.

the horns in the profile arise from different locations in the sky, separated by 10″ in north-south direction. Knapp et al. (1999) interpret these findings in terms of an expanding disk of radius 5×10^{16} cm and thickness 10^{16} cm, inclined by 55° to the line of sight, from which the bulk of the CO emission arises. In their model, the northern part of the disk is tilted away from the observer, it is produced by a constant mass-loss rate of $1.2 \times 10^{-6}\ M_\odot\,\mathrm{yr^{-1}}$ and is expanding in the plane of the disk

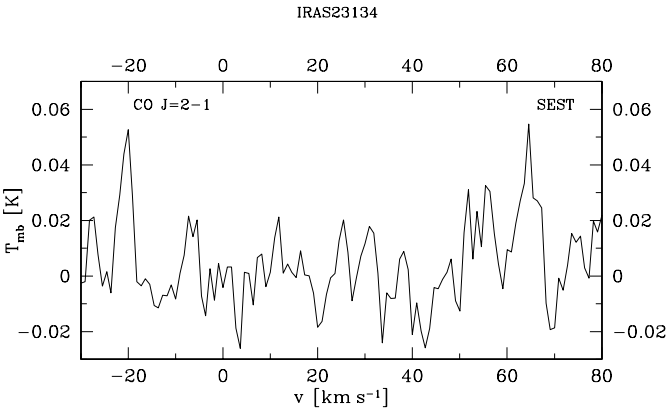

Fig. 24. Low-resolution CO(2–1) spectrum of CC Ind. Note the two features at $-20\,\mathrm{km\,s^{-1}}$ and $+64\,\mathrm{km\,s^{-1}}$, respectively.

with a velocity of $13 \pm 2\,\mathrm{km\,s^{-1}}$ which agrees well with the outflow velocity of the gas in the dense inner region as observed in the SiO(6−5) line. Knapp et al. (1999) do not model the high velocity wind but suggest, that it should arise from the regions toward the poles of the disk. From 60 μm emission, Young et al. (1993b) derive an extent of the dust envelope of $\sim 7 \times 10^{17}$cm and give a mass-loss rate of $\sim 8 \times 10^{-7}\ M_\odot\,\mathrm{yr}^{-1}$ (both values are scaled to the Hipparcos distance of 153 pc). The disk and the bipolar high velocity outflow, therefore, may be embedded in a roughly spherical outer shell.

The presence of these 3 sources in our sample, particularly IRAS 22196–4612, shows that our selection criterion (Valinhos "b" type) is not strict enough to isolate outflows with low velocity and low mass-loss rate.

IRAS 23134−7031 (≡CC Ind): For this source, we found two possible lines at $v_{\mathrm{lsr}} = -20\,\mathrm{km\,s^{-1}}$ and $+64\,\mathrm{km\,s^{-1}}$ (see Fig. 24) in the CO(2–1) spectrum and we did not detect a line in the CO(1–0) spectrum. This source was searched for 86 GHz SiO maser emission by Haikala (1990), but was not detected. Since the radial velocity of CC Ind seems to be presently unknown, we did not use either line in our analysis presented here. Still, the hypothetical wind properties derived from both lines would place the source into the B-regime (see Table 2). From Hipparcos epoch photometry the star was found to be a possible periodic variable with a period $P = 241$ d (Koen & Eyer 2002, their Table 5, CC Ind ≡ HIP 114917).

4.5.4. SiO velocities higher than CO velocities

SiO maser emission at velocities higher than the velocity indicated by the CO(2–1) rotational lines has previously been reported by Cernicharo et al. (1997) and Herpin et al. (1998). In particular, Herpin et al. (1998) find that for the 17 sources of their sample for which they obtained time resolved data, the SiO velocities correlate well with the optical phase of the star, suggesting a connection to the stellar pulsation. This is in excellent agreement with the expectations from our models. In their sample however, the ratio between the SiO velocity width and the full width of the CO line reaches a maximum of only about 1.4 (for S CMi, for which they measure a CO velocity of $3.6\,\mathrm{km\,s^{-1}}$). Also, the high velocity SiO wings in their sample are by about (at least) a factor of ten weaker than the bulk of the SiO emission. This is quite different in L^2 Pup and AY Vir, where the widths of the SiO and CO lines differ by more than a factor of two and where the strength of the high-velocity SiO emission is comparable to the main feature.

5. Discussion

Hydrodynamic models describing pulsating, dust forming circumstellar shells around cool red giant stars have been developed, which include a consistent physical description and numerical modeling of the mutual coupling among hydrodynamics, thermodynamics, chemistry, dust formation and radiative transfer (Fleischer et al. 1992; Winters et al. 1997). Based on this approach, we calculated a grid of about 230 models (i.e. 230 different combinations of the 6 input parameters) for carbon-rich dust forming circumstellar shells (Winters et al. 2000b). Depending on the combination of input parameters, 2 classes of wind models can be distinguished:

A) In the first class of models, radiation pressure on dust dominates the wind generation. These models produce a radiative acceleration $\frac{f^{\mathrm{rad}}}{f^{\mathrm{grav}}} = \alpha > 1$ in the sub-sonic region leading to mass-loss rates in the range of $3 \times 10^{-7} \lesssim \dot{M} \lesssim 10^{-4}\ M_\odot\,\mathrm{yr}^{-1}$ with outflow velocities in the range of $5\,\mathrm{km\,s^{-1}} < v_\infty \lesssim 40\,\mathrm{km\,s^{-1}}$. The radial structure of these models is characterized by discrete dust layers which are accelerated by radiation pressure, leading to the generation of dust induced shocks which propagate through the circumstellar shell. New dust layers are formed on timescales longer than the typical pulsation period of an AGB star. Therefore, the radial structure of the dust shell resembles itself only on a timescale of typically several pulsation periods of the star (e.g., Fleischer et al. 1992; Winters et al. 1994, 1995; Fleischer et al. 1995; Höfner et al. 1995; Winters et al. 2000a).

B) In the models of the second class dust forms, but radiation pressure alone is not sufficient to generate the outflow ($\alpha < 1$ everywhere). These models produce low mass-loss rates $\dot{M} < 3 \times 10^{-7}\ M_\odot\,\mathrm{yr}^{-1}$ and simultaneously low outflow velocities, $v_\infty < 5\,\mathrm{km\,s^{-1}}$. The winds of this class of models are generated by an interplay between the pulsation activity of the underlying star and radiation pressure on dust. The circumstellar shell displays a rather smooth distribution of the hydrodynamic and dust quantities, the radial shell structures do not show major changes in time, but behave almost stationary.

A similar separation of the models into dynamically different regimes is also found in the case of oxygen-rich element compositions (Jeong et al. 2003a) and will be investigated in detail in a forthcoming paper (Jeong et al. 2003b).

In our survey we have detected 59 sources in CO(2–1) out of 65 observed objects. Among them, 10 sources have a narrow profile with a half-width at zero intensity $\leq 5\,\mathrm{km\,s^{-1}}$ and 44 sources have a profile with a half-width $>5\,\mathrm{km\,s^{-1}}$. Additionally, we find in our sample 5 sources showing composite CO profiles with a narrow component (half-width $<5\,\mathrm{km\,s^{-1}}$) superimposed on a broader one (half-width $>5\,\mathrm{km\,s^{-1}}$). The incidence of low velocity outflows in our

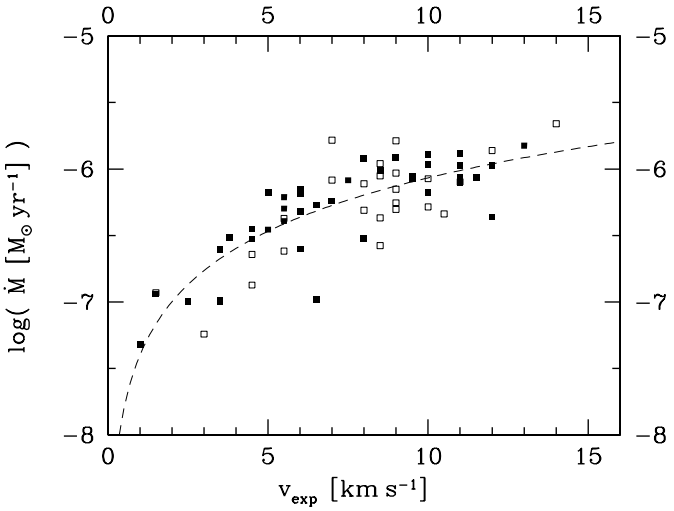

Fig. 25. Mass-loss rates vs. outflow velocity derived from the CO(2–1) lines. Filled squares: IRAM, open squares: SEST. The dashed line shows a least-squares fit to the data in the log-log plane (see text).

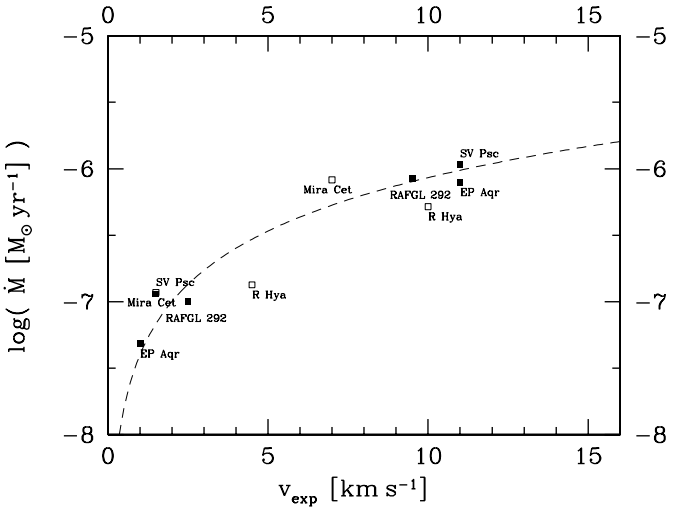

Fig. 26. Mass-loss rates vs. outflow velocities derived from the broad and narrow components of the composite CO(2–1) line profiles. Velocity and mass-loss rate derived from the narrow component of SV Psc and Mira are almost identical. Filled squares: IRAM, open squares: SEST. The dashed line shows the least-squares fit derived for the complete sample.

sample is therefore 15/59 or about 25%. This shows, that our selection criterion is efficient in identifying candidates which might correspond to our B-type models. However, as noted in Sect. 4.5.3, we find in our sample also sources with large outflow velocities (e.g., π^1 Gru with $v_{\rm exp} \sim 15\,{\rm km\,s^{-1}}$) showing, that this criterion should be handled with care. On the other hand we note, that narrow components may be hidden in the broad ones (see, e.g., Fig. 7), so that several sources observed with a broad feature might in fact possess also a low velocity wind. Therefore, the true incidence of low velocity outflows in our sample may be under-evaluated. The identification of such candidates would require profiles with an excellent signal-to-noise ratio.

The separation between the two types of models, A and B, is most obvious in diagrams displaying the mass-loss rate (or the wind momentum ratio, see Winters & Le Bertre 2001) against the radiative acceleration in the dust formation zone. Unfortunately, the radiative acceleration cannot be observed directly nor can it easily be derived from observations.

More easily accessible to observations are the outflow velocities and (more indirect) the mass-loss rates carried by the stellar wind. In Fig. 25 the mass-loss rates are plotted against the outflow velocities for the objects in our sample. Here, we included the values derived from the composite line profiles, assuming two independent wind components. Part of the scatter in the data points should be due to errors in the distances, which we estimate to be accurate within a factor of 2. This factor would translate to a factor 4 in the mass-loss rates. The relation between mass-loss rates and terminal wind velocities derived here from our CO(2–1) observations can be fitted by:

$$\log(\dot{M}[M_\odot\,{\rm yr}^{-1}]) = -7.40 + \frac{4}{3}\log\left(v_{\rm exp}[{\rm km\,s^{-1}}]\right)$$

with a correlation coefficient of 0.82. This fit is shown as dashed line in Figs. 25 and 26. For a velocity of $5\,{\rm km\,s^{-1}}$, this fit to the data results in a mass-loss rate of $3.4\times10^{-7}\,M_\odot\,{\rm yr}^{-1}$, in excellent agreement with the values defining the separation between regions A and B that we found from the model calculations. However, this quantitative agreement should not be overemphasized as we have discussed in Sect. 4.4 that our mass loss rate estimates may be uncertain by a systematic factor. As depicted in Fig. 26, both components of the double winds closely follow the fit relation derived for the whole sample. We note, however, that the values derived for R Hya seem to fall noticeably below the fit line. This may be related to an underestimation of its distance (see Sect. 4.1).

Knapp et al. (1998) find a relation $\dot{M} \propto v^2$ from their sample of CO-bright AGB stars, whereas Young (1995) finds an even steeper slope of $\dot{M} \propto v^{3.35}$ for a sample of optically visible Mira variables within 500 pc of the sun. Olofsson et al. (2002) obtain $\dot{M} \propto v^{1.4}$ for O-rich semiregular and irregular variables and $\dot{M} \propto v^{2.0}$ for C-rich SRs and irregular variables, very close to our result (in our present sample, we have only 2 carbon-stars).

One goal of this investigation is to check, whether we find in nature the objects corresponding to our B-type models. From the B-type models, we expect winds with low outflow velocities and low mass-loss rates. Since our models are pulsating, we also expect high (inward and outward directed) velocities ($\sim$10 km s^{-1}) in the photospheric regions, where the pulsation-generated shock waves are being damped. Therefore, for an object corresponding to a B-type model, we expect narrow profiles of those molecular lines, which are formed far from the star in the wind region and broader, possibly time-dependent, profiles for photospheric emission lines. This is demonstrated in Fig. 27, where the hydrodynamic structure of an oxygen-rich B-type wind model is plotted. The model is characterized by a stellar mass $M_\star = 1\,M_\odot$, luminosity $L_\star = 6500\,L_\odot$, stellar temperature $T_\star = 2200$ K, solar element abundances, i.e. C/O = 0.5, pulsation period $P = 300$ d, and velocity amplitude at the inner boundary $\Delta v_p = 5\,{\rm km\,s^{-1}}$.

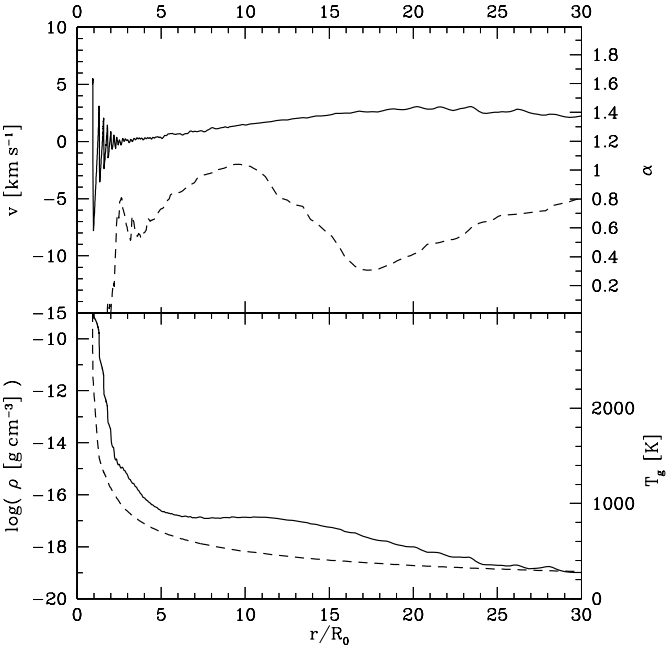

Fig. 27. Hydrodynamic structure of an oxygen-rich B-type model (J75 from Jeong et al. 2003b). Upper panel: hydrodynamic velocity v (solid line, l.h.s. ordinate) and ratio of radiative to gravitational acceleration α (dashed line, r.h.s. ordinate). Lower panel: mass density ρ (solid line, l.h.s. ordinate) and gas temperature $T_{\rm g}$ (dashed line, r.h.s. ordinate).

This model produces a mass-loss rate of $3.1\times10^{-8}\,M_\odot\,{\rm yr}^{-1}$ and an outflow velocity of $3.9\,{\rm km\,s}^{-1}$ (Jeong et al. 2003b). In the photospheric layers, propagating shocks induced by the stellar pulsation dominate the hydrodynamical structure, which should be reflected, e.g., in the SiO 86 GHz maser emission. These shocks are damped out by momentum dissipation to the gas which leads to an increase of the density, allowing a small amount of dust to be formed. The radiative force exerted on the grains however does not exceed the gravitational deceleration. Still, a slow wind is driven by the combination of radiative acceleration and momentum dissipation from the shock waves. The physical conditions in the wind acceleration region should be reflected, e.g., in the 22 GHz water vapor maser line while the CO rotation lines probe the final outflow velocity.

This kind of structure was clearly found in the case of L^2 Pup (Winters et al. 2002). In the present work, we find additional sources (notably AY Vir, but also T Ari, R Peg, RT Hya, and S CMi) which show narrow (one component) CO profiles and (much) broader SiO maser features. Also, among the 5 sources with composite CO profiles we find 4 sources (RAFGL 292, o Cet, EP Aqr, and probably SV Psc) in which the SiO maser indicates photospheric velocities in excess of the wind outflow velocities (for the 5th source, R Hya, we didn't obtain SiO maser data). Therefore, these sources match well the properties expected from the B-type wind models.

From the model calculations we find that there is a sharp transition between the B-regime and the A-regime in terms of the stellar parameters (see Winters et al. 2000b). Thus, if a star situated in this border region undergoes a small change of its parameters, we expect that its wind may "jump" from the B-type to the A-type or vice versa. Therefore, we can expect that there exist objects which are surrounded by two (or even more) successive winds corresponding to type A and B. In our sample we have 5 sources showing composite CO radio line profiles. If these profiles are interpreted in terms of double winds, the mass-loss rates and outflow velocities derived from the narrow and the broad component are typical for our B-type and A-type models, respectively. Also, for each wind component, these values are in perfect agreement with the relation between mass-loss rate and wind velocity that we find from the "single winds" (see Fig. 26), a fact that again lends support to the interpretation of the composite line profiles in terms of double winds. The time a star spends in one of the two wind regimes would depend on the nature of the change in the stellar parameters. A particular example involving two very different time scales is the formation of a detached shell. In Schröder et al. (1998, 1999) it is demonstrated, that a high mass-loss rate episode of short duration could be caused by the increased stellar luminosity following a thermal pulse. When the hydrogen-burning shell resumes its energy production, the star may for a short time surmount a critical luminosity necessary to drive a massive wind. In this case, the star experiences an excursion in the HR diagram, the wind moves from the B-regime to the A-regime. Here it rests for a short time ($\approx$800 yr), and then falls back to the B-regime. At this stage, the star would be surrounded by a double wind: the fast, high mass-loss rate A-type wind would be followed by an inner slow, low mass-loss rate B-type wind. Should the matter that was expelled during the high mass-loss rate episode remain protected from dispersion into the interstellar medium, this wind would show up as a detached shell after some time. The prime example of such an object is the carbon star TT Cyg, which shows a remarkably spherically symmetric CO shell of thickness 2.5 arcsec, separated from the star by 35 arcsec, and expanding at a velocity of $12.6\,{\rm km\,s}^{-1}$ (Olofsson et al. 2000). Assuming that this shell has been formed in a high mass-loss rate episode (rather than by sweeping up a fossil, low density wind), a mass-loss rate of the order of $10^{-5}\,M_\odot\,{\rm yr}^{-1}$ during a period of $\sim$500 yr would be derived (Olofsson et al. 2000). Presently, TT Cyg shows a slow ($\sim3.8\,{\rm km\,s}^{-1}$), low mass-loss rate ($\sim3\times10^{-8}\,M_\odot\,{\rm yr}^{-1}$) wind, typical for the B-type models. In fact, TT Cyg ($K-L'=0.53$, $L'-[12]=1.27$) would fit the selection criteria of our sample. However, the mass-loss rate corresponding to its detached shell is much larger than what we observe in our sample. Also, the CO profiles of TT Cyg and other objects with a detached shell (e.g., S Sct, U Ant) display a distinct double-peaked structure (see, e.g., Olofsson et al. 1993) which we do not find in our spectra. It may therefore be that the events which lead to the formation of clearly detectable detached shells as in the case of TT Cyg are rare (e.g., connected to the thermal pulse time scale), or are specific to carbon stars whereas the formation of multiple winds seems to be a more frequent phenomenon.

Our results suggest, that there are in fact objects corresponding to our B-type models. The models may correspond to a common stage in the evolution of AGB stars, which may have escaped attention because it is not as spectacular as the stages with high mass-loss ($\dot{M}\gtrsim10^{-6}\,M_\odot\,{\rm yr}^{-1}$). A large number of

such objects has been brought to light by the ISOGAL survey of the Galactic Bulge (Omont et al. 1999), where a significant population of low mass-loss rate ($\dot{M} \sim 10^{-8}\ M_{\odot}\,\mathrm{yr}^{-1}$) AGB (or tip-RGB) objects has been revealed. The mass-loss rates of such objects are usually derived from a spectral modeling of their infrared energy distributions, assuming a standard wind velocity of $15\,\mathrm{km\,s}^{-1}$. If these sources would have low velocity outflows ($v_{\mathrm{exp}} \lesssim 5\,\mathrm{km\,s}^{-1}$), as is suggested by our models and also by the presence of a substantial fraction of such sources in our sample, the mass-loss rates of these objects would be over-estimated by at least a factor 3 to 5.

From the 65 sources in our sample, we have observed 39 in the 86 GHz SiO maser and detected 27 of those (15 SRs, 8 Miras, and 4 of unknown variability type), i.e. a fraction of 69%. This detection rate is comparable to the one of 61% in the Galactic Bulge for sources selected from the ISOGAL survey (Messineo et al. 2002). Part of their sample may in fact correspond to the B-type models.

6. Conclusions

We have presented the results of a survey in the CO(2–1), (1–0), and in the SiO($v = 1$, $J = 2$–1) 86 GHz maser line of a sample of 65 AGB stars, selected by their weak near-infrared excess, of which 59 have been detected in CO (2–1).

In our sample we have 10 "single wind" sources with low outflow-velocity and 5 double wind sources, where the narrow component indicates velocities less than $5\,\mathrm{km\,s}^{-1}$. For sources of this type, which make up 25% of our sample, the mass-loss rate would be severely over-estimated, by assuming the standard outflow velocity of $15\,\mathrm{km\,s}^{-1}$ in modeling their infrared spectral energy distributions.

We find several cases with $\Delta v_{\mathrm{SiO}} > \Delta v_{\mathrm{CO}}$. Therefore, the case of L^2 Pup where the effect is spectacular (see Winters et al. 2002) is not unique. This lends support to our interpretation of the slow winds in terms of our "B-type" models. We find this situation also for the narrow component of composite CO profiles. This suggests, that these components may also be interpreted in terms of the "B-type" wind.

We found a case with a triangular shape of the CO profile which can be decomposed into 2 parabolic components (RAFGL 292). The SiO spread in this case is also larger than that of the CO narrow component. This case suggests, that there may be sources where a narrow component could be hidden in the broader one. In order to disentangle these components, high signal-to-noise observations with high velocity resolution are necessary.

We find that the velocities and mass-loss rates derived from the composite CO profiles (interpreting them in terms of two independent wind components) behave exactly as the single winds in a $\dot{M}/v_{\mathrm{exp}}$ diagram. Moreover, the simultaneous presence of broad SiO maser features and narrow CO lines is in excellent agreement with the expectations from consistent hydrodynamical model calculations for spherical winds from pulsating late-type stars. Due to the sensitivity of the wind-type on the stellar parameters in the transition region between regime A and B, the models provide a mechanism for the formation of two (or more) successive winds with very different properties (mass-loss rate and wind velocity) around the same star, caused by small variations of the stellar parameters. In our opinion, these arguments strongly support the interpretation of the composite CO line profiles in terms of successive winds, as proposed by Knapp et al. (1998).

Acknowledgements. We are grateful to Axel Weiss, Frank Bertoldi, and to the flexible pool observers at IRAM, who obtained all the 30 m spectra presented in this work. We also thank Clemens Thum for fruitful suggestions. The referee is thanked for his careful analysis of our work. The calculations were performed on the Cray and NEC computers accessible through the Konrad-Zuse-Zentrum für Informationstechnik Berlin (ZIB) and through the IDRIS, Orsay. This work has been supported by the PROCOPE program under grants D/9822849 (DAAD) and F/01303ZA (MAE). JMW acknowledges financial support by the CNRS. The research by JKS has been supported by a Marie Curie Fellowship of the European Community programme Human Research Potential under contract number HPMF-CT-2000-01041. This research has made use of the SIMBAD database, operated at CDS, Strasbourg, France and of NASA's Astrophysics Data System.

References

Blöcker T. 1999, in AGB stars, ed. T. Le Bertre, A. Lèbre, & C. Waelkens (ASP), IAU Symp., 191, 21
Bowen, G. H. 1988, ApJ, 329, 299
Cernicharo, J., Alcolea, J., Baudry, A., & González-Alfonso, E. 1997, A&A, 319, 607
Cioni, M.-R., Marquette, J.-B., Loup, C., et al. 2003, A&A, 405, 1075
Crocker, D. A., & Hagen, W. 1983, A&AS, 54, 404
Dominik, C., Gail, H.-P., Sedlmayr, E., & Winters, J. M. 1990, A&A, 240, 365
Engels, D., Schmid-Burgk, J., & Walmsley, C. M. 1988, A&A, 191, 283
Epchtein, N., Le Bertre, T., Lépine, J. R. D., et al. 1987, A&AS, 71, 39
Feast, M. W. 1996, MNRAS, 278, 11
Fleischer, A. J., Gauger, A., & Sedlmayr, E. 1992, A&A, 266, 321
Fleischer, A. J., Gauger, A., & Sedlmayr, E. 1995, A&A, 297, 543
Fouqué, P., Le Bertre, T., Epchtein, N., Guglielmo, F., & Kerschbaum, F. 1992, A&AS, 93, 151
Gail, H.-P., & Sedlmayr, E. 1987, A&A, 177, 186
Gérard, E., & Le Bertre, T. 2003, A&A, 397, L17
Gonzalez Delgado, D., Olofsson, H., Kerschbaum, F., Schöier, F. L., & Lindqvist, M. 2003, A&A, submitted
Groenewegen, M. A. T. 1997, A&A, 317, 503
Groenewegen, M. A. T., & Whitelock, P. A. 1996, MNRAS, 281, 1347
Haikala, L. K. 1990, A&AS, 85, 875
Haikala, L. K., Nyman, L.-Å., & Forsström, V. 1994, A&AS, 103, 107
Hall, P. J., Wright, A. E., Troup, E. R., Wark, R. M., & Allen, D. A. 1990, MNRAS, 247, 549
Hashimoto, O., Izumiura, H., Kester, D. J. M., & Bontekoe, T. R. 1998, A&A, 329, 213
Herpin, F., Baudry, A., Alcolea, J., & Cernicharo, J. 1998, A&A, 334, 1037
Höfner, S., Feuchtinger, M. U., & Dorfi, E. A. 1995, A&A, 297, 815
Jeong, K. S., Winters, J. M., Le Bertre, T., & Sedlmayr, E. 2003a, A&A, 407, 191
Jeong, K. S., Winters, J. M., Le Bertre, T., & Sedlmayr, E. 2003b, A&A, submitted
Josselin, E., Mauron, N., Planesas, P., & Bachiller, R. 2000, A&A, 362, 255
Jura, M., Chen, C., & Plavchan, P. 2002, ApJ, 569, 964

Jura, M., & Kahane, C. 1999, ApJ, 521, 302
Kahane, C., & Jura, M. 1994, A&A, 290, 183
Kahane, C., & Jura, M. 1996, A&A, 310, 952
Kastner, J. H. 1992, ApJ, 401, 337
Kemper, F. 2002, Ph.D. Thesis, University of Amsterdam, The Netherlands, available at URL http://cf.uba.uva.nl/nl/publicaties/kemper/
Kerschbaum, F., & Olofsson, H. 1999, A&AS, 138, 299
Kerschbaum, F., Olofsson, H., & Hron, J. 1996, A&A, 311, 273
Kholopov, P. N., Samus', N. N., Frolov, M. S., et al. 1985, General Catalogue of Variable Stars, 4th ed. (Moscow: Nauka)
Knapp, G. R., & Morris, M. 1985, ApJ, 292, 640
Knapp, G. R., Pourbaix, D., Platais, I., & Jorissen, A. 2003, A&A, 403, 993
Knapp, G. R., Young, K., & Crosas, M. 1999, A&A, 346, 175
Knapp, G. R., Young, K., Lee, E., & Jorissen, A. 1998, ApJS, 117, 209
Koen, C., & Eyer, L. 2002, MNRAS, 331, 45
Le Bertre, T. 1997, A&A, 324, 1059
Le Bertre, T., Matsuura, M., Winters, J. M., et al. 2001, A&A, 376, 997
Lebzelter, T., & Hinkle, K. H. 2002, A&A, 393, 563
Ledoux, P. 1958, Handbuch der Physik, vol. LI, Astrophysik II, Stellar Stability, ed. S. Flügge (Berlin: Springer), 605
Ledoux, P., & Walraven, T. 1958, Handbuch der Physik, vol. LI, Astrophysik II, Variable stars, ed. S. Flügge (Berlin: Springer), 353
Loup, C., Forveille, T., Omont, A., & Paul, J. F. 1993, A&AS, 99, 291
Mamon, G. A., Glassgold, A. E., & Huggins, P. J. 1988, ApJ, 328, 797
Margulis, M., Van Blerkom, D. J., Snell, R. L., & Kleinmann, S. G. 1990, ApJ, 361, 673
Messineo, M., Habing, H., Sjouwerman, L., Omont, A., & Menten, K. 2002, A&A, 393, 115
Morris, M., Lucas, R., & Omont, A. 1985, A&A, 142, 106
Nguyen-Q-Rieu, Bujarrabal, V., Olofsson, H., Johnsson, L. E. B., & Turner, B. E. 1984, ApJ, 286, 276
Nyman, L.-Å., Booth, R. S., Carlström, U., et al. 1992, A&AS, 93, 121
Olofsson, H., Bergman, P., Lucas, R., et al. 2000, A&A, 353, 583
Olofsson, H., Eriksson, K., Gustafsson, B., & Carlström, U. 1993, ApJS, 87, 267
Olofsson, H., González Delgado, D., Kerschbaum, F., & Schöier, F. L. 2002, A&A, 391, 1053
Omont, A., Ganesh, S., Alard, C., et al. 1999, A&A, 348, 755
Ostlie, D. A., & Cox, A. N. 1986, ApJ, 311, 864
Patel, N. A., Joseph, A., & Gaulsan, R. 1992, J. Astrophys. Astr., 13, 241
Richichi, A., Fabbroni, L., Ragland, S., & Scholz, M. 1999, A&A, 344, 511
Ryde, N., & Schöier, F. L. 2001, ApJ, 547, 384
Sahai, R. 1992, A&A, 253, L33
Schöier, F. L., & Olofsson, H. 2001, A&A, 368, 969
Schröder, K.-P., Winters, J. M., Arndt, T. U., & Sedlmayr, E. 1998, A&A, 335, L9
Schröder, K.-P., Winters, J. M., & Sedlmayr, E. 1999, A&A, 349, 898
van der Veen, W. E. C. J., & Habing, H. J. 1988, A&A, 194, 125
Winters, J. M., Fleischer, A. J., Gauger, A., & Sedlmayr, E. 1994, A&A, 290, 623
Winters, J. M., Fleischer, A. J., Gauger, A., & Sedlmayr, E. 1995, A&A, 302, 483
Winters, J. M., Fleischer, A. J., Le Bertre, T., & Sedlmayr, E. 1997, A&A, 326, 305
Winters, J. M., Keady, J. J., Gauger, A., & Sada, P. V. 2000a, A&A, 359, 651
Winters, J. M., Le Bertre, T., Jeong, K. S., Helling, C., & Sedlmayr, E. 2000b, A&A 361, 641
Winters, J. M., & Le Bertre, T. 2001, in Post-AGB objects as a phase of stellar evolution, ed. R. Szczerba, & S.K. Górny (Kluwer), 93
Winters, J. M., Le Bertre, T., Nyman, L.-Å., Omont, A., & Jeong, K. S. 2002, A&A, 388, 609
Wood, P. R. 1979, ApJ, 227, 220
Young, K. 1995, ApJ, 445, 872
Young, K., Phillips, T. G., & Knapp, G. R. 1993a, ApJS, 86, 517
Young, K., Phillips, T. G., & Knapp, G. R. 1993b, ApJ, 409, 725